



**HAL**  
open science

## Mapping Hidden Residual Structure within the Myc bHLH-LZ Domain Using Chemical Denaturant Titration

Panova Stanislava, Matthew J Cliff, Pavel F Macek, Martin Blackledge, Malene Ringkjøbing Jensen, Nissink Willem M, Kevin J Embrey, Davies Rick, Jonathan P. Waltho

### ► To cite this version:

Panova Stanislava, Matthew J Cliff, Pavel F Macek, Martin Blackledge, Malene Ringkjøbing Jensen, et al.. Mapping Hidden Residual Structure within the Myc bHLH-LZ Domain Using Chemical Denaturant Titration. *Structure*, 2019, 27 (10), pp.1537-1546.e4. 10.1016/j.str.2019.07.006 . hal-03016176

**HAL Id: hal-03016176**

<https://hal.univ-grenoble-alpes.fr/hal-03016176v1>

Submitted on 26 Nov 2020

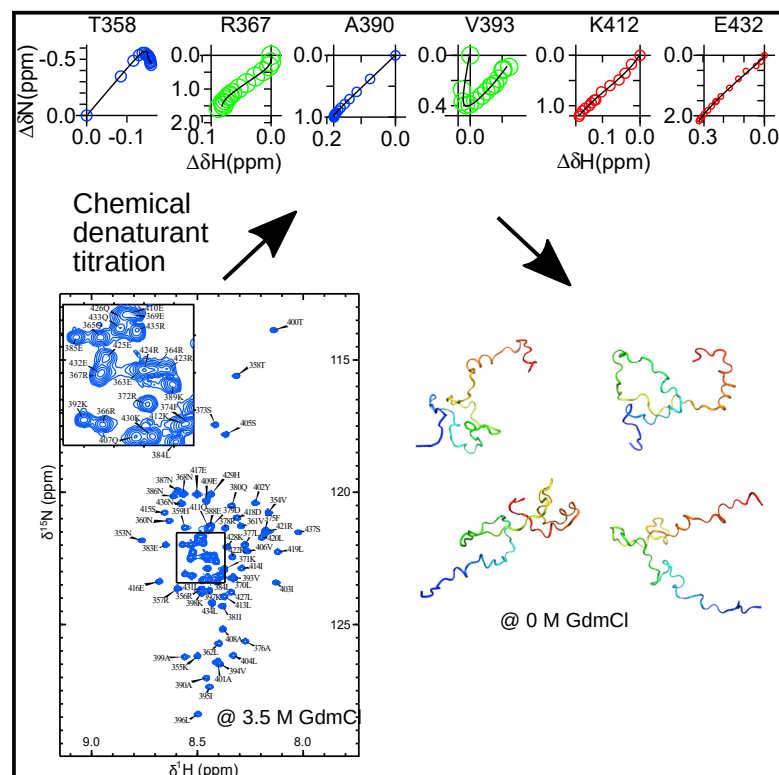
**HAL** is a multi-disciplinary open access archive for the deposit and dissemination of scientific research documents, whether they are published or not. The documents may come from teaching and research institutions in France or abroad, or from public or private research centers.

L'archive ouverte pluridisciplinaire **HAL**, est destinée au dépôt et à la diffusion de documents scientifiques de niveau recherche, publiés ou non, émanant des établissements d'enseignement et de recherche français ou étrangers, des laboratoires publics ou privés.

# Structure

## Mapping Hidden Residual Structure within the Myc bHLH-LZ Domain Using Chemical Denaturant Titration

### Graphical Abstract



### Authors

Stanislava Panova, Matthew J. Cliff, Pavel Macek, ..., Kevin J. Embrey, Rick Davies, Jonathan P. Waltho

### Correspondence

j.waltho@manchester.ac.uk

### In Brief

We apply chemical denaturant titration (CDT)-NMR to the bHLH-LZ domain of the oncoprotein Myc to determine the secondary structure propensities and tertiary interactions for all residues in the domain, including those with poor NMR properties under native conditions, and define the regions perturbed by a small-molecule inhibitor.

### Highlights

- Developed the chemical denaturant titration-NMR techniques
- Secondary and tertiary structures are determined for residues with poor NMR properties
- Sites perturbed by the inhibitor, 10058-F4, map to areas of Myc with residual structure



# Mapping Hidden Residual Structure within the Myc bHLH-LZ Domain Using Chemical Denaturant Titration

Stanislava Panova,<sup>1</sup> Matthew J. Cliff,<sup>1</sup> Pavel Macek,<sup>2,3</sup> Martin Blackledge,<sup>4</sup> Malene Ringkjøbing Jensen,<sup>4</sup> J. Willem M. Nissink,<sup>5</sup> Kevin J. Embrey,<sup>2</sup> Rick Davies,<sup>2</sup> and Jonathan P. Waltho<sup>1,6,7,\*</sup>

<sup>1</sup>Manchester Institute of Biotechnology, University of Manchester, Manchester M1 7DN, UK

<sup>2</sup>Discovery Sciences, IMED Biotech Unit, AstraZeneca, Alderley Park SK10 4TG, UK

<sup>3</sup>NMR-Bio, Institut de Biologie Structurale, Grenoble Cedex 9, France

<sup>4</sup>Univ. Grenoble Alpes, CNRS, CEA, IBS, 38000 Grenoble, France

<sup>5</sup>Oncology, IMED Biotech Unit, AstraZeneca, Cambridge CB2 0AA, UK

<sup>6</sup>Molecular Biology and Biotechnology, University of Sheffield, Sheffield S10 2TN, UK

<sup>7</sup>Lead Contact

\*Correspondence: [j.waltho@manchester.ac.uk](mailto:j.waltho@manchester.ac.uk)

<https://doi.org/10.1016/j.str.2019.07.006>

## SUMMARY

Intrinsically disordered proteins (IDPs) underpin biological regulation and hence are highly desirable drug-development targets. NMR is normally the tool of choice for studying the conformational preferences of IDPs, but the association of regions with residual structure into partially collapsed states can lead to poor spectral quality. The bHLH-LZ domain of the oncoprotein Myc is an archetypal example of such behavior. To circumvent spectral limitations, we apply chemical denaturant titration (CDT)-NMR, which exploits the predictable manner in which chemical denaturants disrupt residual structure and the rapid exchange between conformers in IDP ensembles. The secondary structure propensities and tertiary interactions of Myc are determined for all bHLH-LZ residues, including those with poor NMR properties under native conditions. This reveals conformations that are not predictable using existing crystal structures. The CDT-NMR method also maps sites perturbed by the prototype Myc inhibitor, 10058-F4, to areas of residual structure.

## INTRODUCTION

Intrinsically disordered regions of proteins or entire intrinsically disordered proteins (IDPs) are extremely prevalent in higher eukaryotes, and are involved in a wide range of biologically important processes, such as extracellular communication, intracellular signaling, and DNA replication and transcription (Babu et al., 2011; Habchi et al., 2014; Oldfield and Dunker, 2014; Wright and Dyson, 2015). The conformational ensemble defined as disordered does not necessarily represent a purely random coil state, and different IDP sequences exhibit different behaviors, ranging from rapidly rearranging disordered coils, to more

collapsed states with long-range contacts and persistent secondary structure elements. These latter IDPs can be classified as having molten globule-like behavior, characterized by a loose core without the precise packing of folded proteins (van der Lee et al., 2014). Molten globule-like behavior is observed in a range of states from native-like folds with dynamic interiors (e.g., apomyoglobin), to ensembles with low hydrodynamic radii but no persistent structure. IDPs that display this behavior are frequently involved in molecular recognition, and some adopt conventional globular structures when in complex with a binding partner. The basic-helix-loop-helix-leucine zipper (bHLH-LZ) domain of the oncoprotein Myc is an archetypal example of such behavior.

Myc is an important transcription factor for cell growth, metabolism, and apoptosis, and its overexpression is associated with many cancers (Santarius et al., 2010). Transcriptional activity of Myc requires hetero-dimerization with the protein Max. Both proteins have disordered bHLH-LZ domains, which become ordered upon heterodimer formation, leading to the recognition and binding of the E-box DNA sequence (Blackwood and Eisenman, 1991; Nair and Burley, 2003; Prendergast et al., 1991). This makes small-molecule inhibitors that disrupt the Myc-Max interaction attractive candidates to be used as anticancer agents (Follis et al., 2009; Metallo, 2010), but their development is limited by a lack of appropriate characterization of Myc in the IDP state adopted when isolated from Max.

Conventional structural biology techniques are not well-suited for IDPs, because any tertiary structure is transient. NMR spectroscopy provides a number of informative measurements, including chemical shifts, residual dipolar couplings (RDCs), and paramagnetic relaxation enhancement (PRE) (Bhowmick et al., 2017; Jensen et al., 2014; Sormanni et al., 2017). PREs report on interactions up to 30 Å, and on rarely populated states (<5%) (Baldwin and Kay, 2009; Clore, 2013; Salmon et al., 2010). However, IDPs present challenges to standard NMR techniques; low structural complexity results in poor signal dispersion, although this is ameliorated by the intense resonances observed for fully denatured proteins, and exposed amide groups are subject to signal loss through solvent exchange, although this can sometimes be ameliorated using <sup>13</sup>C-detection (Bermel et al.,



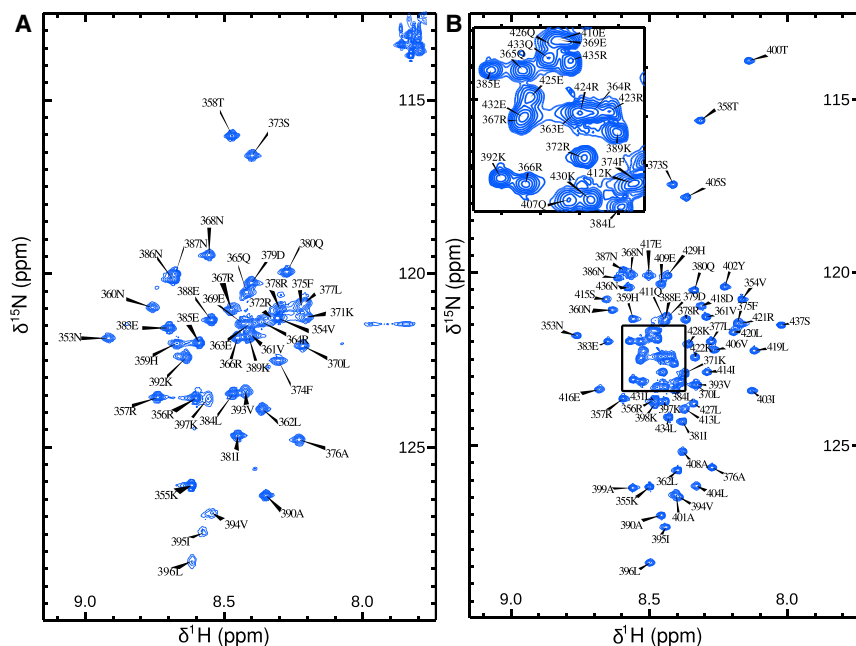


**Figure 1.  $^1\text{H}$ - $^{15}\text{N}$  HSQC Spectra of Myc bHLH-LZ Domain**

(A) under the standard buffer conditions and 0 M GdmCl.

(B) under the standard buffer conditions with addition of GdmCl to 3.2 M. Amide cross peaks are labeled with the residue number and single letter code for their assigned amino acid. No peaks are visible in spectrum (A) for residues 400–437. Inset in (B) shows the crowded region marked with a box in the center of the spectrum.

native-like conditions (20 mM phosphate, 0.1 M NaCl pH 7.4, 298K) shows only 46 out of 83 possible cross peaks (Figure 1A). The detected peaks are broad, while retaining the poor dispersion expected of a fully disordered protein. Therefore, residual order is slowing motion to a timescale that causes the intensity of some resonances to be completely attenuated by NMR relaxation. Changes in NaCl concentration, pH, and acquisition temperature failed to increase the number of detected peaks (described in the STAR Methods).

In contrast, introduction of chemical denaturant substantially improved the spectra. All 83 expected backbone amide signals are observable at 0.6 M GdmCl and above, and all resonances have narrow linewidths (<14 Hz for  $^1\text{H}$ ) at 3.2 M GdmCl (Figure 1B).

Residue-specific assignment of all backbone amide resonances was completed at 3.2 M GdmCl using conventional triple-resonance experiments, and an additional (H)N(CA)NNH experiment for regions where the  $C_\alpha$  dispersion is poor. The  $^1\text{H}_\text{N}$  and  $^{15}\text{N}_\text{H}$  chemical shifts were observed to change continuously in a titration from 3.2 to 0 M GdmCl, allowing the assignment to be transferred to other GdmCl concentrations. HNCACB spectra were recorded at 2.4, 1.6, and 0 M of GdmCl to verify the assignment at these GdmCl concentrations. The resonances that are missing in the absence of GdmCl correspond to the C-terminal residues of Myc (400–437), and constitute part of the second helix (H2) and the whole LZ region in the Myc-Max crystal structure (secondary structure shown in Figure 2A).

### Three Categories of Response to Denaturant

The responses of the NMR resonances to GdmCl were categorized into three distinct behavior types (Figures 2A and 2B). For some residues (blue category, Figures 2A and 2B), the largest chemical shift changes occur at low GdmCl concentration (<0.6 M) where both  $\delta^1\text{H}_\text{N}$  and  $\delta^{15}\text{N}_\text{H}$  have the same hyperbolic relationship with GdmCl concentration. These transitions correspond well with the behavior when GdmCl is replaced by NaCl in the titrations (Figure S1). Hence, the effect is independent of the cation present and therefore is ascribed to interaction with  $\text{Cl}^-$  ions. The simplest model of a binding interaction is adequate to describe the data, but the interaction with  $\text{Cl}^-$  may not be a direct binding event, and may also involve formation of Myc homodimers (Blackwood and Eisenman, 1991). For a second group

2012; Goradia et al., 2015; Wiedemann et al., 2015). IDPs that have molten globule-like behavior are more problematic, because the underlying conformational exchange typically occurs on timescales that result in severely attenuated NMR resonances. The signal attenuation is proposed to arise from averaging between many conformers with a large range of barrier heights defined by a rough protein conformation energy landscape (Milanesi et al., 2012).

Here, the structure propensity of the isolated bHLH-LZ domain from Myc has been extensively characterized using CDT-NMR. Under native-like conditions, the molten globule-like behavior of Myc results in residues of the LZ region producing no detectable resonances. We resolve this problem by shifting the solution equilibrium toward a monomeric, less-collapsed state (McParland et al., 2002; Reed et al., 2006); titration with increasing guanidinium chloride (GdmCl) induces a cooperative transition of Myc to a more disordered state. The GdmCl dependence is used to extrapolate chemical shifts back to native conditions and to analyze the PREs of three singly S-(1-oxyl-2,2,5,5-tetramethyl-2,5-dihydro-1H-pyrrol-3-yl)methyl methanesulfonothioate (MTSL)-labeled cysteine variants. The data reveal considerable helical structure under native conditions, especially in part of the LZ region. There is also significant tertiary contact between residues in the helix 2-LZ boundary region and those of helix 1 that is quite different to that observed in the Myc-Max crystal structure (Nair and Burley, 2003). The CDT-NMR approach also allows the interaction with the prototype Myc inhibitor, 10058-F4, to be identified as specifically affecting this tertiary contact in the molten globule-like state of Myc.

## RESULTS

### Assignment of bHLH-LZ Domain NMR Spectra

The  $^{15}\text{N}$ - $^1\text{H}$  heteronuclear single quantum coherence (HSQC) spectra of the bHLH-LZ domain of Myc (residues 352–437) in

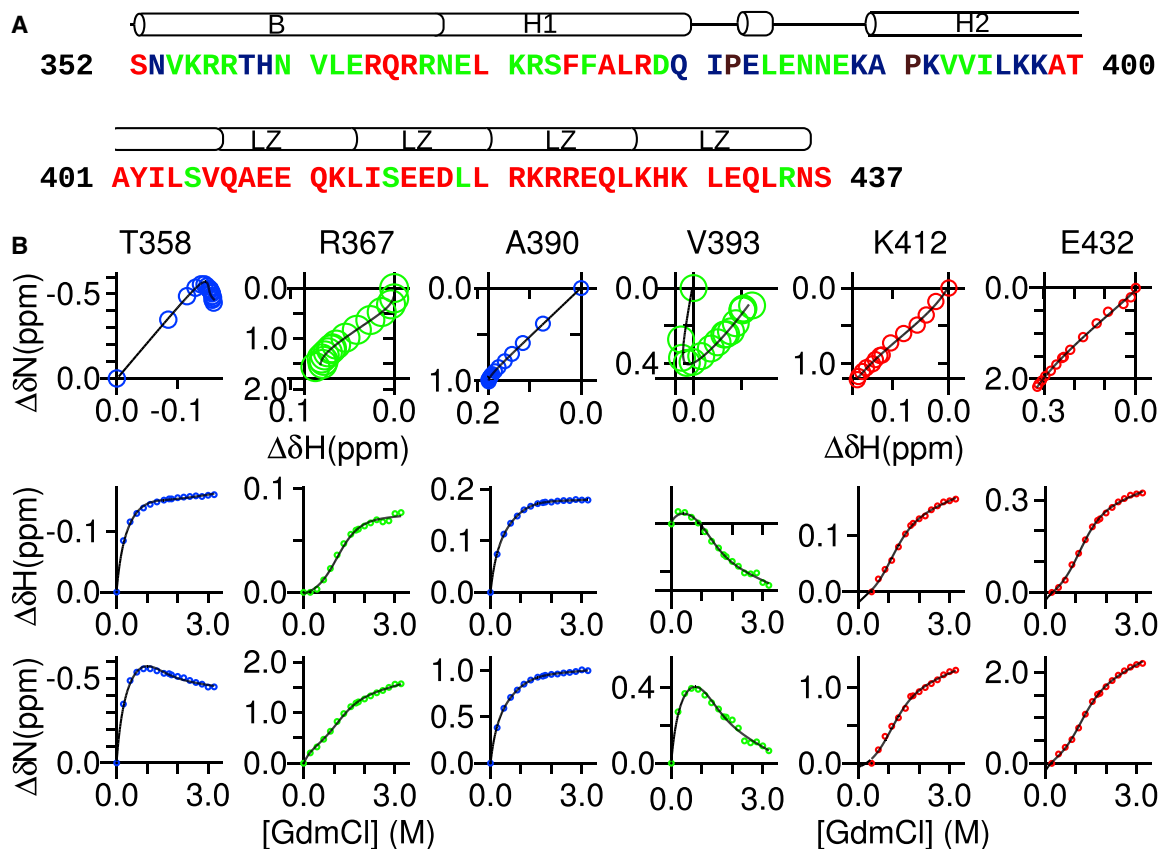


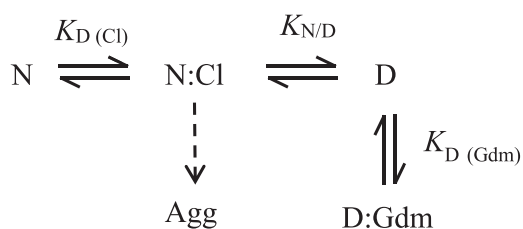
**Figure 2. Response of Myc to Denaturant**

(A) Primary structure of Myc bHLH-LZ domain with residues color coded according to category of behavior, mostly hyperbolic (blue), mostly sigmoidal (red), and showing both transitions (green), with the secondary structure boundaries taken from the Myc-Max crystal structure PDB:1NKP (B, basic helix; H1, helix 1; H2, helix 2; LZ, leucine zipper heptad repeats). Circle radii reflect the uncertainty in the chemical shift measurements (0.005 ppm for  $\delta^1\text{H}_\text{N}$  and 0.02 ppm for  $\delta^{15}\text{N}_\text{H}$ ). (B) Titration behavior of amide crosspeaks for a selection of residues. The top row shows positional changes in  $^1\text{H}$ - $^{15}\text{N}$  HSQC spectra with the axes origin indicating the starting chemical shift (lowest concentration of GdmCl giving a visible peak). The middle and bottom rows show  $\delta^1\text{H}_\text{N}$  and  $\delta^{15}\text{N}_\text{H}$  (respectively) behavior as a function of GdmCl concentration. Solid lines show behavior expected from the best-fit parameters generated by a global fit to Equation 1 (see the STAR Methods), where chemical shift-related parameters are varied for each residue, but underlying physical constants reflect the whole protein. The best-fit global parameters are  $K_{\text{ND}} = 14 \pm 3$  ( $-6.2 \pm 0.4$  kJ mol $^{-1}$ ),  $m = -2.8 \pm 0.2$  ( $6.5 \pm 0.4$  kJ mol $^{-1}$  M $^{-1}$ ), and  $K_{\text{D}(\text{Cl})} = 410 \pm 40$  mM ( $14$  kJ mol $^{-1}$ ). The mean  $\chi^2$  was 12.9 with 24 degrees of freedom.

of residues (red category, Figures 2A and 2B), the  $\delta^1\text{H}_\text{N}$  and  $\delta^{15}\text{N}_\text{H}$  changes have a sigmoidal dependence on GdmCl concentration with a mid-point at  $\sim 1.2$  M. There is no equivalent transition with NaCl and so the effect is ascribed to the Gdm $^+$  ions and is indicative of a folding event with some cooperativity. A third group of residues (green category, Figures 2A and 2B) is subject to both effects and, in contrast to the other categories, these  $^1\text{H}$ - $^{15}\text{N}$  crosspeaks follow a significantly curved path as the denaturant concentration changes. In addition, all residues show a weak linear dependence on GdmCl concentration, which persists at high denaturant concentrations ( $>2.5$  M). This likely reflects a weak interaction between Gdm $^+$  and the protein backbone (Plaxco et al., 1997), analogous to the well-established effect of urea (Huang et al., 2012; Meier et al., 2007). The total reaction scheme for the interaction between Myc and GdmCl is described by Scheme 1: where N stands for native disordered state of Myc, D for denatured, and N:Cl and D:Gdm indicate the bound forms. The dotted arrow represents a very slow pre-

cipitation of Myc in the presence of elevated Cl $^-$  concentrations, which is countered by Gdm $^+$  ions.

The parameters defining the Cl $^-$  interaction and the cooperative folding event were fitted globally to Equation 1 using  $\delta^1\text{H}_\text{N}$  and  $\delta^{15}\text{N}_\text{H}$  values for a subset of residues with large chemical shift changes, and then fixed when fitting the chemical shift changes for all residues. All residues are fitted satisfactorily with global parameters for the underlying physical processes (examples in Figure 2B). Fitting the chemical shift changes using the global parameters allows the extrapolation of the incomplete datasets to 0 M GdmCl, thereby providing estimates of  $\delta^1\text{H}_\text{N}$  and  $\delta^{15}\text{N}_\text{H}$  values where none could be determined experimentally. The accuracy of these estimates was determined to be 0.03 ppm for  $\delta^1\text{H}_\text{N}$  and 0.3 ppm for  $\delta^{15}\text{N}_\text{H}$  (see the STAR Methods). Using  $\Delta\delta^1\text{H}_\text{N}$  and  $\delta^{15}\text{N}_\text{H}$  values in the global fitting procedure rather than the standard chemical shift perturbation formula ( $(\Delta\delta^1\text{H}_\text{N}^2 + (\Delta\delta^{15}\text{N}_\text{H}/6)^2)^{0.5}$ ) produced more consistent fit parameter values, particularly for residues in the green category



**Scheme 1. Reaction Scheme for the Interaction Between Myc and GdmCl**

(Figure 2B), because the root-sum of squares function does not account for the direction of chemical shift changes.

The sequence distribution of the resulting chemical shift changes corresponding to each transition is shown in Figure S2. The derived  $K_{\text{D}}$  value for the interaction with  $\text{Cl}^-$  (410 mM) is consistent with weak, non-specific binding, which is focused at hotspots around the KRR sequence (residues 355–357) and around residue A390, which in the Myc-Max crystal structure correspond to the N-terminal basic H1 region and the turn region, respectively. The signal attenuation observed at low denaturant concentration precluded analysis of the  $\text{Cl}^-$  interaction for much of the C-terminal region. The best-fit parameters for the cooperative folding transition indicate weak stability ( $-6.2 \text{ kJ mol}^{-1}$ ) and a low  $\text{Gdm}^+$   $m$ -value of 2.8 (equivalent to  $6.5 \text{ kJ mol}^{-1} \text{ M}^{-1}$  (Clarke and Waltho, 1997; Myers et al., 1995)) for the more folded species; values typical of partially ordered states (Cliff et al., 2009; Reed et al., 2006; Scholtz et al., 2009). The final two heptad repeats of the LZ (residues 426–436) in the Myc-Max crystal structure show the largest chemical shift changes for this transition, and are in the region with large signal attenuations in native-like conditions. The gradients of the weak linear dependence of chemical shift on GdmCl concentration, visible at high denaturant concentrations, are also largest for the C-terminal residues.

### The $\alpha$ -Helical Structure Is Populated at Low Denaturant Concentrations

The changes in chemical shift with denaturant suggest that the conformational distribution of the polypeptide chain is changing. Whereas some of these changes can be ascribed to weak interactions with  $\text{Cl}^-$  or  $\text{Gdm}^+$ , the cooperative transition is consistent with structural changes that alter the exposure of hydrophobic surface area (Scholtz et al., 2009). The backbone  $^1\text{H}$ ,  $^{15}\text{N}$ , and  $^{13}\text{C}$  chemical shifts were analyzed to determine whether these changes corresponded to a change in secondary structure propensity (SSP). Full datasets ( $\delta^{15}\text{N}_{\text{H}}$ ,  $\delta^{15}\text{N}_{\text{H}}$ ,  $\delta^{13}\text{C}_{\alpha}$ , and  $\delta^{13}\text{C}_{\beta}$ ) were available at 1.6, 2.4, and 3.2 M GdmCl, with additional data at 0 M for residues 352–395. The  $\Delta\delta^{13}\text{C}$  values have a strong correlation with  $\Delta\delta^{15}\text{N}_{\text{H}}$  values for the same residue (Figure S3) and so  $\delta^{13}\text{C}_{\alpha}$  and  $\delta^{13}\text{C}_{\beta}$  were extrapolated back to 0 M GdmCl using the fitted  $\Delta\delta^{15}\text{N}_{\text{H}}$  values from the analysis above, which allowed estimation of SSPs for residues 400–437. The accuracy of the extrapolations was determined to be 0.23 ppm for both  $\delta^{13}\text{C}_{\alpha}$  and  $\delta^{13}\text{C}_{\beta}$  (see the STAR Methods).

Two helical clusters can be distinguished (residues 359–373 and 400–436), which dissolve upon addition of GdmCl (Figure 3). In particular, the region from residues 416 to 422 (SEEDLLR) is predicted to be 90% helical in the absence of denaturant. These

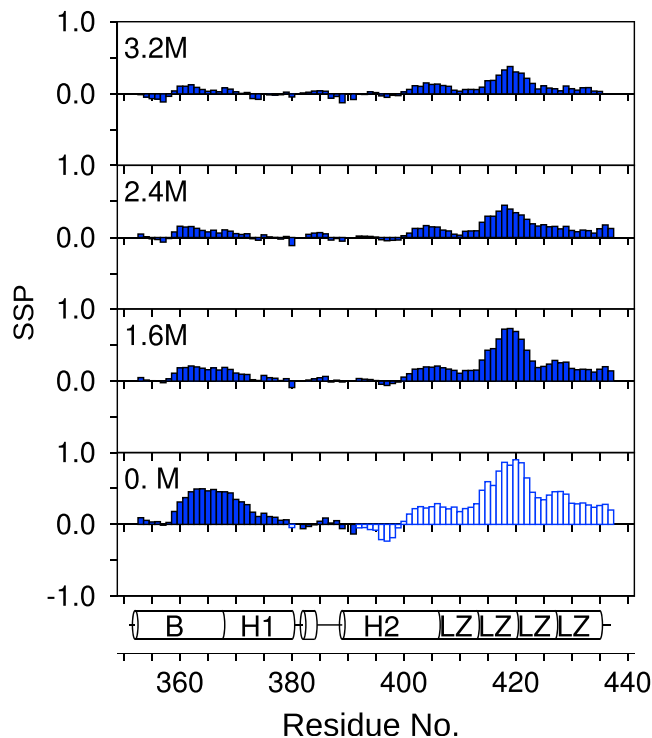


**Figure 3. Secondary Structure Prediction**

Predictions from SSP on the basis of  $^{13}\text{C}_{\alpha}$  and  $^{13}\text{C}_{\beta}$  chemical shifts, at the labeled denaturant concentrations. Positive values indicate helix, and negative values indicate  $\beta$  strand or PPII helix. Filled bars show predictions based on measured chemical shifts, whereas predicted values for residues lost through signal broadening are shown as open bars.

clusters are also helical in the Myc-Max crystal structure. However, the reverse is not always true; for example, the residues of the first turn of H2 in the Myc-Max crystal structure (393–396, VVIL) have a significant strand or PPII-helix propensity in isolated Myc at 0 M GdmCl. The chemical shifts for several residues do not reach random coil values at 3.2 M GdmCl, with up to 30% helical content remaining in the LZ region. It is notable that the region of greatest helix content determined from  $\delta^{13}\text{C}$  values does not co-locate to the region of greatest  $\delta^{15}\text{N}_{\text{H}}$  perturbation by GdmCl (Figure S2), which lies between residue Q426 and the C terminus.

### Paramagnetic Relaxation Enhancements Detect a Tertiary Contact at Low Denaturant

The secondary structure information present in chemical shifts is complemented by tertiary contact information from PRE measurements. A number of single-cysteine variants were screened for optimal protein expression, and three were prepared and labeled using the nitroxide spin-label MTSL, namely Q365C-SL, N386C-SL, and S405C-SL. The denaturant titration profiles for the derivatized variants are very similar to the equivalent profiles for wild-type Myc (Figure S4), with crosspeaks being readily assigned by direct comparison of spectra. In the absence of denaturant, no data are available for residues 400–437 because of the signal attenuation described above. To gain tertiary contact information from the line-broadened peaks, PREs were



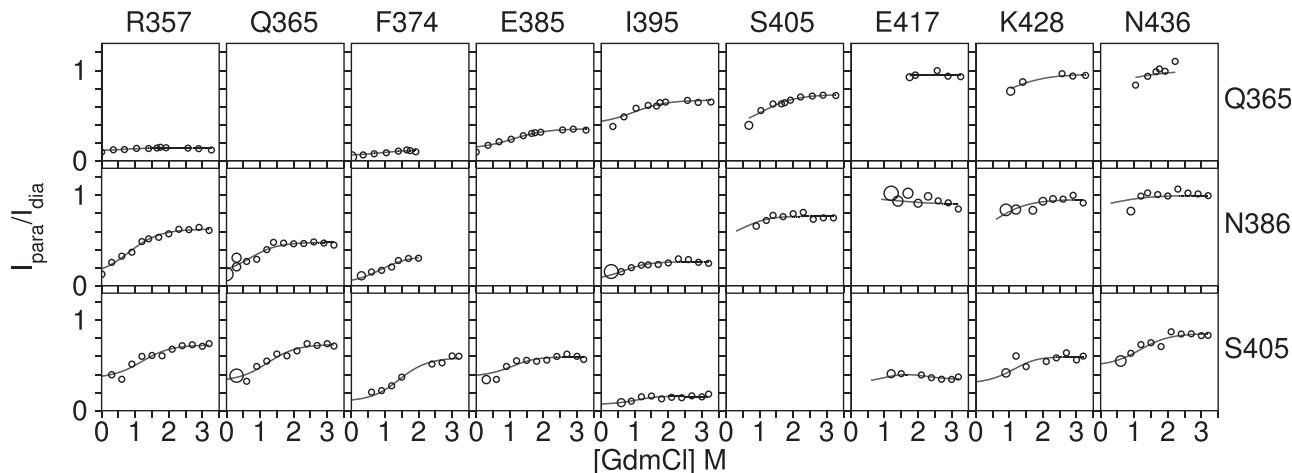


**Figure 4. Denaturant Dependence of PREs for Example Residues**

Best-fit relationships for Equation 2 are shown as solid lines. Crosspeak intensity ratios between paramagnetic and diamagnetic samples are shown as circles, with the radii showing the calculated errors.

measured as a function of denaturant concentration, and Equation 2 was used to extrapolate PRE values for residues with attenuated signals at 0 M GdmCl, using the parameters defined by the analysis of chemical shift changes (Cliff et al., 2009) (see Figure 4 for example profiles).

For all three spin-labeled variants, there is a strong denaturant dependence for the measured PREs. At 0 M GdmCl (Figure 5A), the sequence distribution of the resulting intensity ratios ( $I_{\text{para}}/I_{\text{dia}}$ ) is broad. The Q365C-SL variant reports significant contacts throughout the 355–390 region, with lower effects up to residue Q407, but little contact with the C-terminal region. The N386C-SL variant reports contacts throughout the same region, with the primary effect occurring between residues Q365 and A399. In contrast, the S405C-SL variant reports contacts over much more of the sequence, with the primary effects broadly centered around residue F375 and, to a lesser extent, around residue E425. Effects observed for residues before Q365 and between E385 and A390 are lower, indicating there is a preferential contact between S405 and the F375 region compared with the intervening residues. At 3.2 M GdmCl (Figure 5B), the PREs from each spin-labeled variant largely follow the behavior expected for a fully disordered protein, but with some low PREs (i.e., intensity ratios less than 2 SD below that expected for a random coil) at sequence distant positions. The Q365C-SL variant reports contacts extending to K355 and Q407, while the N386C-SL variant reports contacts to the region between residues Q365 and R378. The S405C-SL variant reports contacts to the region between residues E363 and E385. Hence, the simplest model is that the observed PREs at this GdmCl concentration reflect the rare population of species that resemble the native disordered state.

Overall, the primary long-range contacts detected in the native disordered state are consistent between the three spin-label variants and occur between regions around F375 and around T400, and between around L370 and around E385. The former contact is close to an intramolecular contact within Myc present in the Myc-Max crystal structure, where the C terminus of H1 interacts with H2. In order to test how consistent the measured PREs are

with this folded state of Myc, values were calculated on the basis of an isolated Myc monomer from the crystal structure conformation, and a modeled Myc homodimer (using Max as a template) (solid lines in Figure 5A). This established that the native disordered state of Myc is a much more dynamic system as the PRE data are, in general, inconsistent with ordered, folded states; the calculated profiles for folded Myc show significant peaks and troughs throughout the sequence (blue line in Figure 5A). For the Q365-SL variant, the distribution of PREs is very different to the calculated values, particularly around residues A390 and S415, indicating substantial non-native character. However, for the S405-SL variant, the distribution, although not the size, of PREs more closely resembles the calculated values from the folded structures.

The NMR properties exhibited by the native disordered state of Myc may reflect transient intramolecular or intermolecular interactions, or a combination of both. Consistent with a self-association component, the broadening of resonances for LZ residues showed a small dependence on protein concentration below 1.2 M GdmCl. Consequently, PREs were measured as a function of protein concentration to determine the extent to which intermolecular contacts contributed to the native disordered state. Changes in intensity ratios of less than 10% were observed upon 10-fold dilution (Figure S5). In addition, MTSL-derivatized  $^{14}\text{N}$  Myc had a negligible PRE effect on the NMR spectrum of underivatized  $^{15}\text{N}$ -labeled Myc, at the lowest GdmCl concentration where all peaks were visible (Figure S6). Therefore, the protein concentration dependence of signal intensities of LZ residues is ascribed to viscosity or other solvent effects rather than self-association, and the dominant relaxation enhancements and chemical shift changes result from intramolecular contacts.

### The Structure of the bHLH-LZ Domain Is Compact and Disordered

To visualize the properties of an ensemble that is consistent with the data, and to allow calculation of macroscopic properties like the radius of gyration ( $R_g$ ), the experimental PREs and chemical shifts were used as input into flexible meccano/ASTEROIDS

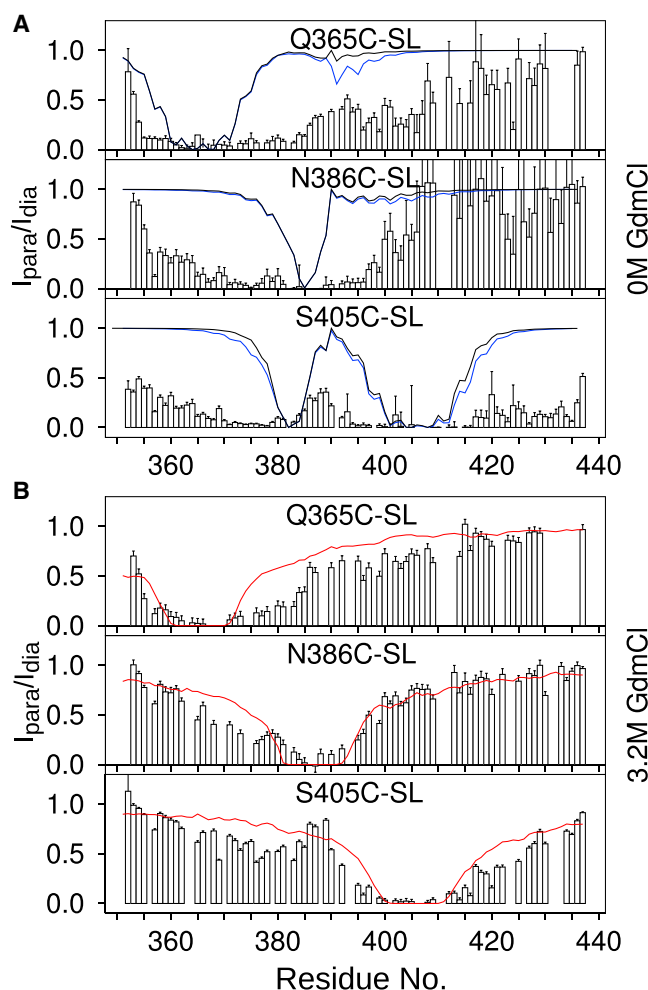


**Figure 5. Calculated Paramagnetic Relaxation Enhancements**

Sequence distribution of PREs ( $I_{\text{para}}/I_{\text{dia}}$ ) at 0 M (A) and 3.2 M GdmCl (B), for each spin-labeled variant. For residues that experience significant line-broadening (400–417), values at 0 M GdmCl were based on the fits of denaturation profiles to Equation 2. Error bars are standard deviations calculated by propagating the noise in the 2D spectra. In (A), the solid lines show the behavior expected for the Myc-Max crystal structure monomer (black) and a modeled homodimer (blue). In (B), the red solid line shows the behavior expected for a self-excluding random coil with the sequence-specific secondary structure propensity (an ensemble generated by flexible mecanno/ASTERIODS).

calculations (Ozenne et al., 2012; Salmon et al., 2010). The extensive degrees of freedom available to IDPs vastly outweigh the sparse experimental constraints, so the resulting ensemble does not reliably predict chemical shift and PRE data other than those used as input. An initial pool of 10,000 conformers was calculated based on the extrapolated chemical shift values ( $^{13}\text{C}_{\alpha}$ ,  $^{13}\text{C}_{\beta}$ ,  $^1\text{H}_N$ , and  $^1\text{N}$ ) at 0 M GdmCl. Five ensembles of 200 conformers that satisfied both the chemical shift and PRE data were then selected from the initial pool using ASTEROIDS, and combined into a final ensemble.

The calculated values for the final ensemble correspond well to the experimental ones (Figure S7). Per residue secondary structure propensities in the final ensemble (example Ramachandran plots are shown in Figure 6A) are consistent with the

SSP predictions above (Figure 3) and show that two main regions of  $\psi, \phi$  space dominate,  $\alpha$ -helical and PPII (Figure 6B). The  $\beta$  strand region is less populated, with just one residue, I381, predominantly (~60%) in this conformation. The 416–421 region shows almost 100%  $\alpha$  helicity, in close agreement SSP predictions based solely on chemical shift.

The contact map and the distribution of  $R_g$  values calculated from the final ensembles (Figures 6C and 6D) illustrate that residues in the 360–380 region are closer to residues in the 400–410 region than would be expected for a random coil ensemble, consistent with the experimental PRE data (Figure 5). Correspondingly, the  $R_g$  distribution peaks at 23 Å, which is 5 Å smaller than in the distribution for the initial pool. The compaction is not as large as for the formation of the Myc-Max crystal structure ( $R_g = 18$  Å), and, whereas there are some preferential conformations, the ensemble is largely disordered. Representative protein conformations (Figure 7) illustrate the distribution of helical segments, and the absence of common tertiary structure.

### Structure in Relation to Ligand Binding

A number of molecules that specifically interact with Myc have been reported (Metallo, 2010), but thus far their mode of interaction has been difficult to define (Follis et al., 2008; Hammoudeh et al., 2009; Harvey et al., 2012; Heller et al., 2017). Hence, we investigated whether the CDT-NMR approach could help elucidate the interactions of a molten globule-like IDP with a ligand. The archetypal Myc-targeting molecule, 10058-F4, has an anti-proliferative action in cell cultures that is consistent with interrupting the Myc-Max interaction (Yin et al., 2003). Initial NMR studies under native conditions showed some signs of interaction between the measurable resonances of Myc and 10058-F4, but these effects were small, meaning that other solvent effects such as protein and DMSO concentration variations could not be discounted. Therefore, the experiments were repeated at Gdm<sup>+</sup> concentrations at which there is significant population of the molten globule-like state, but the population of the denatured state produces more favorable NMR relaxation behavior and therefore higher spectral quality.

For this system, the optimal conditions were 0.5 M GdmCl, at which the equilibrium position is 80% molten globule-like and 20% denatured, according to the best-fit parameters for the data in Figure 2B. Under these conditions, 10058-F4 induces significant attenuation of  $^1\text{H}$ - $^{15}\text{N}$  HSQC crosspeaks, although only minor chemical shift changes (Figure 8A), consistent with slow intermediate exchange. However, whereas the distribution of affected residues is quite broad (Figure 8B), it has a pattern that resembles the PRE profiles (Figure 5), rather than one that resembles the transition between the denatured and molten globule-like states. The greatest loss of intensity is at a region around T400 (shown as isolated orange peaks in Figure 8B), with a weaker effect at residues 360–380. In contrast, residues from K420 onward are relatively unaffected. This is consistent with the interaction between 10058-F4 and Myc specifically stabilizing the previously identified weak tertiary interaction between the 360–380 and 400–410 regions (Figure 5), rather than stabilizing all regions with molten globule-like behavior. The concentration of 10058-F4 is low (1 mM), so the most probable mechanism is by a specific direct interaction with Myc rather than a solvent effect. The region showing greatest intensity



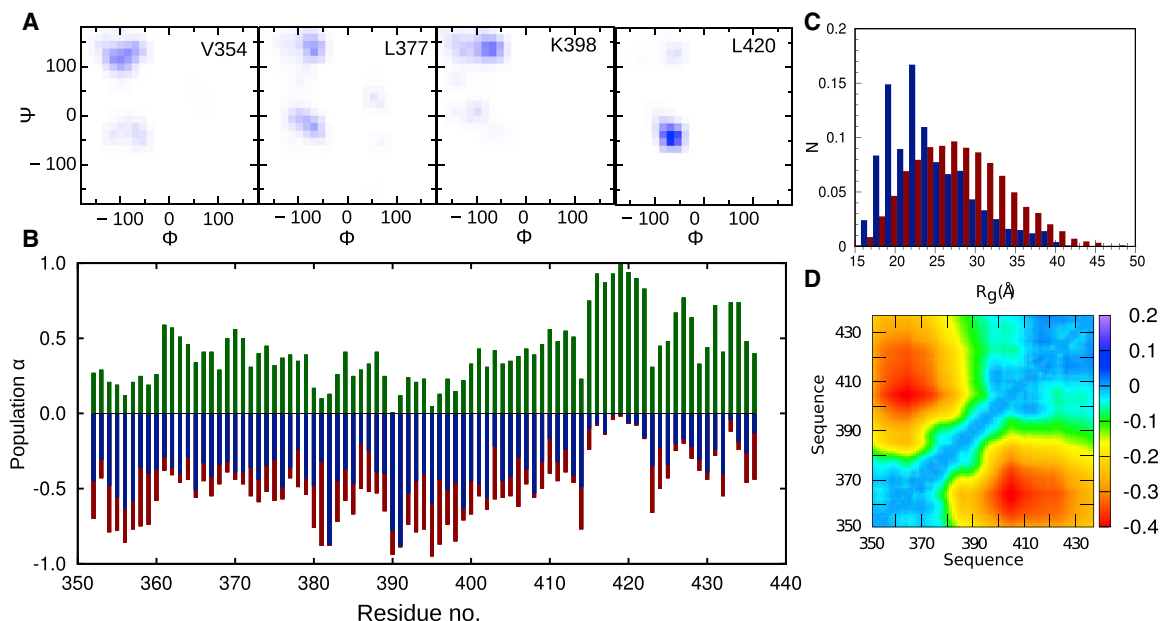


**Figure 6. Structural Parameters for the Ensemble Selected by ASTEROIDS**

(A) Ramachandran plots showing the amino acid conformational potentials for representative residues V354, L377, K398, and L420 in the ensemble.

(B) Populations of residues in the ensemble with dihedral angles in particular regions of Ramachandran space:  $\alpha$  helix (green), PPII (dark blue), and  $\beta$  strand (red), with the PPII and  $\beta$  regions being summed and defined as negative. The number of conformers populating the left-handed helix was negligibly small for all residues (<3%). Definition of regions of Ramachandran space was done as described previously (Ozenne et al., 2012).

(C) Distribution of radius of gyration ( $R_g$ ) for the random coil (red) and the final PRE, chemical shift-based ensemble (blue).  $R_g$  for the random coil state is 29 Å and decreases to 28 Å when the chemical shifts are included in calculations. Inclusion of PRE data reduces this to 23 Å, a compaction of 82%. The compaction expected from the Myc-Max crystal structure is 58%.

(D) Final contact map showing Myc long-range contacts derived using chemical shift and PRE data. Heatmap represented in terms of log-ratio of the distance between residues in the selected and chemical shift-based pool  $\Delta_{ij} = \log(\langle d_{ij} \rangle / \langle d_{ij,ref} \rangle)$ . Colors range from red (−0.4, regions in closer contact than pool; see the STAR Methods) to blue (0.0) to violet (0.2, regions farther apart than pool).

loss corresponds to one that has complete signal attenuation under native conditions (Figure 1A), making it difficult to identify using standard NMR approaches. No interaction is apparent at GdmCl concentrations above 0.8 M, due to the low population of residual structure, indicating that the optimal Gdm<sup>+</sup> concentration to investigate ligand binding in different systems will firstly need to be established using CDT-NMR.

## DISCUSSION

Previous work on chemically denatured proteins demonstrated that they rapidly interconvert between denatured states with random coil behavior and more compact, molten globule-like states, with the population of the more compact forms increasing as conditions become more native-like (Candotti et al., 2013; Cliff et al., 2009; Schulman et al., 1997). NMR measurements reflect the average behavior of the ensemble, and measurements under a range of conditions can allow the contribution of sub-populations to be deconvolved. Molten globule-like states frequently have very poor NMR characteristics, with low resonance dispersion and fast relaxation (leading to broad resonances and signal attenuation), and so the CDT method allows the determination of otherwise hidden behavior. The data here show that the Myc bHLH-LZ domain is an IDP with such molten globule-like behavior. The per residue folding parameters associated with the regions of Myc with high struc-

ture propensity are similar enough that chemical shift data for all residues can be fitted with common values, but the parameters do not necessarily describe a transition between states that is concomitant across the molecule. They are more likely to reflect that individual local clusters have similar hydrophobic burial and stability, but mostly form independently of each other.

Previous NMR studies of Myc behavior have used viral isoforms (v-Myc; Fieber et al., 2001), variants with some or all of the bHLH-LZ region missing (B-Myc; Burton et al., 2006), or short peptides derived from the Myc sequence (Hammoudeh et al., 2009; Lavigne et al., 1998). Such studies can be argued not to fully represent the behavior of the wild-type protein in conditions most relevant to the cellular environment, and to small-molecule-based intervention in disease states. In this study, significant helical propensity is seen throughout the Myc sequence, and matches well the helical regions identified in v-Myc (Fieber et al., 2001) and short peptides. Furthermore, the method has also allowed PRE measurements to determine longer-range interactions and give a fuller description of the structure propensity of the domain. The ensemble calculation suggests that no particular conformation dominates, but the average  $R_g$  is considerably smaller than for a random coil. The tertiary contacts in the ensemble are consistent with the results of a recent molecular dynamics study, which suggest that Myc has a tendency to form a hairpin-like conformation (Liu et al., 2017).

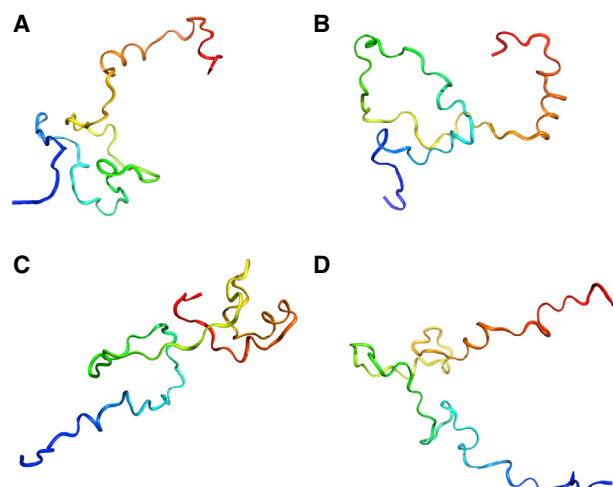


**Figure 7. Representative Structures from the Final Ensemble Selected by ASTEROIDS**

(A) Lowest  $R_g$  conformer, (B) most frequently selected conformer, (C) closest to mean  $R_g$  conformer, and (D) mode  $R_g$  conformer. Structures are represented as a ribbon colored blue to red, N to C termini. Consistent helical region is in the orange region.

The structural elements defined for Myc in the absence of denaturant are potentially functionally important. The region with the greatest helical content (>90% helical; residues 416–422, Figure 3) corresponds to the position within the LZ that is important in ensuring specificity for the interaction with Max, and mutation of residues E417, R423, and R424 results in significant homodimerization (Soucek et al., 1998). The long-range tertiary contact defined by the PREs (between the 360–380 and 400–410 regions) coincides with the phosphorylation sites S373 and T400 (Macek et al., 2018), suggesting that phosphorylation perturbs this conformational ensemble, leading to its role in the mechanism of gene regulation. In addition, mutation of R367 is sufficient to allow homodimerization (Beaulieu et al., 2012), an effect that is ascribed to electrostatic repulsion, but might be caused by the stabilization of non-native contacts. Furthermore, the regions of tertiary contacts coincide with the regions that are affected by the small-molecule inhibitor, 10058-F4, suggesting that a similar regulatory effect can be induced by pharmaceuticals, and holds hope for the design of further drug candidate molecules.

Non-random coil behavior in disordered protein chains is well-established, both for conventionally folded proteins (N-PGK [Cliff et al., 2009], Drk-SH 3 [Marsh et al., 2007], Staph Nuclease [Zhang et al., 1997]), and for IDPs. For example, our results broadly resemble those obtained with spin-labeled variants of  $\alpha$ -synuclein (Bertoncini et al., 2005; Dedmon et al., 2005), which in combination with RDCs, defined tertiary interactions to be present in the absence of denaturant, and that contribute even at 8 M Urea. The interactions are between the C terminus and the aggregation prone NAC region of  $\alpha$ -synuclein. Studies with Tau show it to have both compact and extended regions (Schwalbe et al., 2014), whereas the contact map for Myc shows higher level of compactness for most regions of the construct. On the basis of these studies with Tau and  $\alpha$ -synuclein, a link was pro-

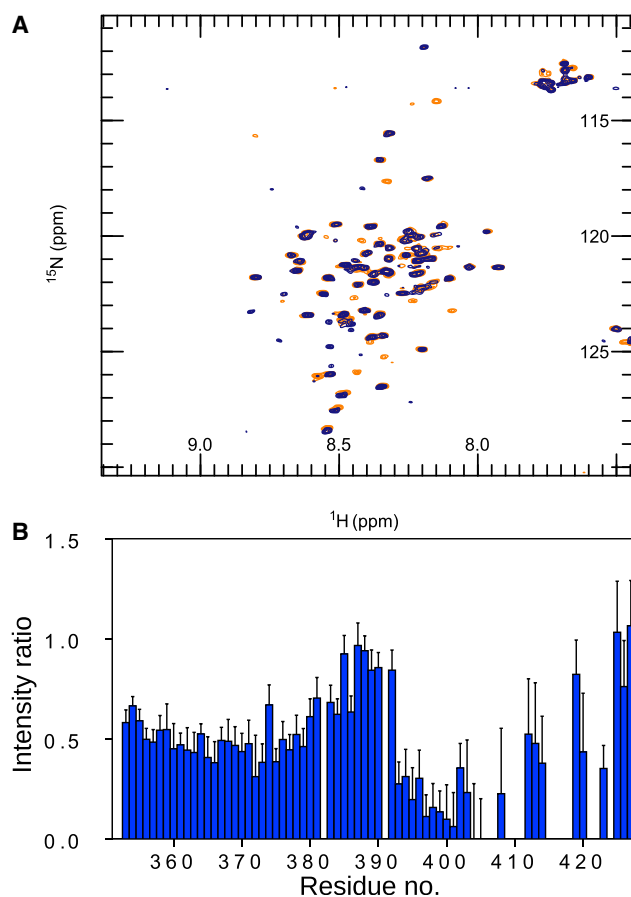


**Figure 8. Ligand Binding at 0.5 M GdmCl**

(A) HSQC spectra of 100  $\mu$ M Myc recorded at 0.5 M GdmCl and 5% DMSO- $d_6$ , in the presence (dark blue) and absence (orange) of 1 mM 10058-F4. (B) Ratio of peak height for assigned resonances in the two spectra, showing regions of Myc affected by the compound. Error bars are standard deviations calculated by propagating the noise in the 2D spectra.

posed between polyproline II propensity and aggregation prone precursors for pathogenic  $\beta$  strand formation, but whereas there are polyproline II-favored regions in Myc, which coincide with the loop in Myc-Max crystal structure, the NMR data show they are not prone to aggregation.

In conclusion, CDT-NMR has allowed us to explore fully the conformational ensemble of a wild-type protein domain containing all the elements required to interact with its binding partners, Max and DNA, despite many resonances being broadened beyond detection in the absence of denaturant, and others having little or no intensity in triple-resonance spectra. The application of the CDT method extends from previous Myc studies by allowing the delineation of native behavior from that of the chemically denatured state. The utility of the CDT-NMR method for regions that have poor spectral properties in the absence of denaturant has allowed the behavior of the LZ region to be determined, which has not been possible using previous methods. The signals that are most attenuated by conformational exchange are inherently those with the strongest structure propensity. It follows from the conventional structure-function paradigm that such regions are most likely to be functionally significant (as

here, the most structured region defines Myc-Max specificity) and, potentially, the most druggable. Even in fuzzy complexes, in which the structure-function paradigm does not apply so rigorously, specificity is likely to be defined by small clusters of transient structure. Having defined the denaturant dependence of structured regions, a system can be poised at an equilibrium position where the contribution from more compact conformers is significant, but not sufficient to attenuate the NMR signals deleteriously. This approach can be used, for example, to delineate interactions with inhibitors, making IDPs with molten globule-like behavior amenable to hitherto prohibited screening of lead drug compounds. The method should also be compatible with other NMR measurements such as RDCs, and the identification of protein-protein interactions.

## STAR★METHODS

Detailed methods are provided in the online version of this paper and include the following:

- KEY RESOURCES TABLE
- LEAD CONTACT AND MATERIALS AVAILABILITY
- EXPERIMENTAL MODEL AND SUBJECT DETAILS
- METHOD DETAILS
- QUANTIFICATION AND STATISTICAL ANALYSIS
  - Ensemble Calculation
- DATA AND CODE AVAILABILITY

## SUPPLEMENTAL INFORMATION

Supplemental Information can be found online at <https://doi.org/10.1016/j.str.2019.07.006>.

## ACKNOWLEDGMENTS

S.P. was supported through a President's Doctoral Scholar Award of the University of Manchester funded jointly by Bruker, and through BBSRC award K016245. P.M. was an AZ-funded post-doctoral researcher. All data were recorded at Manchester Biomolecular NMR facility.

## AUTHOR CONTRIBUTIONS

S.P. produced and purified the protein, performed NMR experiments, analyzed the data, and wrote the paper. M.J.C. designed experiments, analyzed the data, and wrote the paper. P.M. designed protein constructs, carried out NMR experiments, and analyzed the data. M.R.J. and M.B. performed the structural ensemble selections using ASTEROIDS. J.W.M.N., K.J.E., and R.D. designed and coordinated experiments. J.P.W. supervised the project. All authors discussed results and commented on the manuscript.

## DECLARATION OF INTERESTS

J.W.M.N., K.J.E., and R.D. are employees of the AstraZeneca and may have stock/stock options in AstraZeneca.

Received: November 26, 2018

Revised: May 5, 2019

Accepted: July 17, 2019

Published: August 8, 2019

## REFERENCES

Babu, M.M., van der Lee, R., de Groot, N.S., and Gsponer, J. (2011). Intrinsically disordered proteins: regulation and disease. *Curr. Opin. Struct. Biol.* *21*, 432–440.

Baldwin, A.J., and Kay, L.E. (2009). NMR spectroscopy brings invisible protein states into focus. *Nat. Chem. Biol.* *5*, 808–814.

Beaulieu, M.E., McDuff, F.O., Frappier, V., Montagne, M., Naud, J.F., and Lavigne, P. (2012). New structural determinants for c-Myc specific heterodimerization with Max and development of a novel homodimeric c-Myc b-HLH-LZ. *J. Mol. Recognit.* *25*, 414–426.

Bermei, W., Bertini, I., Chill, J., Felli, I., Haba, N., Kumar, M., and Pierattelli, R. (2012). Exclusively heteronuclear (<sup>13</sup>C)-detected amino-acid-selective NMR experiments for the study of intrinsically disordered proteins (IDPs). *Chembiochem* *13*, 2425–2432.

Bertoncini, C.W., Jung, Y.-S., Fernandez, C.O., Hoyer, W., Griesinger, C., Jovin, T.M., and Zweckstetter, M. (2005). Release of long-range tertiary interactions potentiates aggregation of natively unstructured  $\alpha$ -synuclein. *Proc. Natl. Acad. Sci. U S A* *102*, 1430–1435.

Bhowmick, A., Brookes, D.H., Yost, S.R., Dyson, H.J., Forman-Kay, J.D., Gunter, D., Head-Gordon, M., Hura, G.L., Pande, V.S., Wemmer, D.E., et al. (2017). Finding our way in the dark proteome. *J. Am. Chem. Soc.* *138*, 9730–9742.

Blackwood, E.M., and Eisenman, R.N. (1991). Max: a helix-loop-helix zipper protein that forms a sequence-specific DNA-binding complex with Myc. *Science* *251*, 1211.

Burton, R.A., Mattila, S., Taparowsky, E.J., and Post, C.B. (2006). B-Myc: N-terminal recognition of Myc binding proteins. *Biochemistry* *45*, 9857–9865.

Candotti, M., Esteban-Martín, S., Salvatella, X., and Orozco, M. (2013). Toward an atomistic description of the urea-denatured state of proteins. *Proc. Natl. Acad. Sci. U S A* *110*, 5933–5938.

Clarke, A.R., and Waltho, J.P. (1997). Protein folding pathways and intermediates. *Curr. Opin. Biotechnol.* *8*, 400–410.

Cliff, M.J., Craven, C.J., Marston, J.P., Hounslow, A.M., Clarke, A.R., and Waltho, J.P. (2009). The denatured state of N-PGK is compact and predominantly disordered. *J. Mol. Biol.* *385*, 266–277.

Clare, G.M. (2013). Generating accurate contact maps of transient long-range interactions in intrinsically disordered proteins by paramagnetic relaxation enhancement. *Biophys. J.* *104*, 1635–1636.

Dedmon, M.M., Lindorff-Larsen, K., Christodoulou, J., Vendruscolo, M., and Dobson, C.M. (2005). Mapping long-range interactions in  $\alpha$ -synuclein using spin-label NMR and ensemble molecular dynamics simulations. *J. Am. Chem. Soc.* *127*, 476–477.

Fieber, W., Schneider, M.L., Matt, T., Krautler, B., Konrat, R., and Bister, K. (2001). Structure, function, and dynamics of the dimerization and DNA-binding domain of oncogenic transcription factor v-Myc. *J. Mol. Biol.* *307*, 1395–1410.

Follis, A.V., Hammoudeh, D.I., Daab, A., and Metallo, S.J. (2009). Small-molecule perturbation of competing interactions between c-Myc and Max. *Bioorg. Med. Chem. Lett.* *19*, 807–810.

Follis, A.V., Hammoudeh, D.I., Wang, H., Prochownik, E.V., and Metallo, S.J. (2008). Structural rationale for the coupled binding and unfolding of the c-Myc oncoprotein by small molecules. *Chem. Biol.* *15*, 1149–1155.

Goradia, N., Wiedemann, C., Herbst, C., Görlach, M., Heinemann, S.H., Ohlenschläger, O., and Ramachandran, R. (2015). An approach to NMR assignment of intrinsically disordered proteins. *Chemphyschem* *16*, 739–746.

Habchi, J., Tompa, P., Longhi, S., and Uversky, V.N. (2014). Introducing protein intrinsic disorder. *Chem. Rev.* *114*, 6561–6588.

Hammoudeh, D.I., Follis, A.V., Prochownik, E.V., and Metallo, S.J. (2009). Multiple independent binding sites for small-molecule inhibitors on the oncoprotein c-Myc. *J. Am. Chem. Soc.* *131*, 7390–7401.

Harvey, S.R., Porrini, M., Stachl, C., MacMillan, D., Zinzalla, G., and Barran, P.E. (2012). Small-molecule inhibition of c-MYC: MAX leucine zipper formation is revealed by ion mobility mass spectrometry. *J. Am. Chem. Soc.* *134*, 19384–19392.

Heller, G.T., Aprile, F.A., Bonomi, M., Camilloni, C., De Simone, A., and Vendruscolo, M. (2017). Sequence specificity in the entropy-driven binding of a small molecule and a disordered peptide. *J. Mole. Biol.* *429*, 2772–2779.

Huang, J.-r., Gabel, F., Jensen, M.R., Grzesiek, S., and Blackledge, M. (2012). Sequence-specific mapping of the interaction between urea and unfolded

- ubiquitin from ensemble analysis of NMR and small angle scattering data. *J. Am. Chem. Soc.* **134**, 4429–4436.
- Jensen, M.R., Zweckstetter, M., Huang, J.-R., and Blackledge, M. (2014). Exploring free-energy landscapes of intrinsically disordered proteins at atomic resolution using NMR spectroscopy. *Chem. Rev.* **114**, 6632–6660.
- Lavigne, P., Crump, M.P., Gagné, S.M., Hodges, R.S., Kay, C.M., and Sykes, B.D. (1998). Insights into the mechanism of heterodimerization from the <sup>1</sup>H-NMR solution structure of the c-Myc-Max heterodimeric leucine zipper. *J. Mol. Biol.* **287**, 165–181.
- Liu, J., Dai, J., He, J., Niemi, A.J., and Ilieva, N. (2017). Multistage modeling of protein dynamics with monomeric Myc oncoprotein as an example. *Phys. Rev. E* **95**, 032406.
- Macek, P., Cliff, M.J., Embrey, K.J., Holdgate, G.A., Nissink, W.M., Panova, S., Waltho, J.P., and Davies, R.A. (2018). Myc phosphorylation in its basic helix-loop-helix region destabilizes transient  $\alpha$ -helical structures, disrupting Max and DNA binding. *J. Biol. Chem.* **293**, 9301–9310.
- Marsh, J.A., Neale, C., Jack, F.E., Choy, W.Y., Lee, A.Y., Crowhurst, K.A., and Forman-Kay, J.D. (2007). Improved structural characterizations of the drkN SH3 domain unfolded state suggest a compact ensemble with native-like and non-native structure. *J. Mol. Biol.* **367**, 1494–1510.
- McParland, V.J., Kalverda, A.P., Homans, S.W., and Radford, S.E. (2002). Structural properties of an amyloid precursor of  $\beta_2$ -microglobulin. *Nat. Struct. Biol.* **9**, 326–331.
- Meier, S., Grzesiek, S., and Blackledge, M. (2007). Mapping the conformational landscape of urea-denatured ubiquitin using residual dipolar couplings. *J. Am. Chem. Soc.* **129**, 9799–9807.
- Metallo, S.J. (2010). Intrinsically disordered proteins are potential drug targets. *Curr. Opin. Chem. Biol.* **14**, 481–488.
- Milanesi, L., Waltho, J.P., Hunter, C.A., Shaw, D.J., Beddard, G.S., Reid, G.D., Dev, S., and Volk, M. (2012). Measurement of energy landscape roughness of folded and unfolded proteins. *Proc. Natl. Acad. Sci. U S A* **109**, 19563.
- Myers, J.K., Pace, C.N., and Scholtz, J.M. (1995). Denaturant *m* values and heat capacity changes: relation to changes in accessible surface areas of protein unfolding. *Protein Sci.* **4**, 2138–2148.
- Nair, S.K., and Burley, S.K. (2003). X-Ray structures of Myc-Max and Mad-Max recognizing DNA: molecular bases of regulation by proto-oncogenic transcription factors. *Cell* **112**, 193–205.
- Oldfield, C.J., and Dunker, A.K. (2014). Intrinsically disordered proteins and intrinsically disordered protein regions. *Annu. Rev. Biochem.* **83**, 553–584.
- Ozenne, V., Schneider, R., Yao, M.X., Huang, J.R., Salmon, L., Zweckstetter, M., Jensen, M.R., and Blackledge, M. (2012). Mapping the potential energy landscape of intrinsically disordered proteins at amino acid resolution. *J. Am. Chem. Soc.* **134**, 15138–15148.
- Plaxco, K.W., Morton, C.J., Grimshaw, S.B., Jones, J.A., Pitkeathly, M., Campbell, I.D., and Dobson, C.M. (1997). The effects of guanidine hydrochloride on the 'random coil' conformations and NMR chemical shifts of the peptide series GGXGG. *J. Biomol. NMR* **10**, 221–230.
- Prendergast, G.C., Lawe, D., and Ziff, E.B. (1991). Association of Myn, the murine homolog of Max, with c-Myc stimulates methylation-sensitive DNA binding and ras cotransformation. *Cell* **65**, 395–407.
- Reed, M.A.C., Jelinska, C., Syson, K., Cliff, M.J., Splevins, A., Alizadeh, T., Hounslow, A.M., Staniforth, R.A., Clarke, A.R., Craven, C.J., et al. (2006). The denatured state under native conditions: a non-native-like collapsed state of N-PGK. *J. Mol. Biol.* **357**, 365–372.
- Salmon, L., Nodet, G., Ozenne, V., Yin, G., Jensen, M.R., Zweckstetter, M., and Blackledge, M. (2010). NMR characterization of long-range order in intrinsically disordered proteins. *J. Am. Chem. Soc.* **132**, 8407–8418.
- Santarius, T., Shipley, J., Brewer, D., Stratton, M.R., and Cooper, C.S. (2010). A census of amplified and overexpressed human cancer genes. *Nat. Rev. Cancer* **10**, 59–64.
- Scholtz, J.M., Grimsley, G.R., and Pace, C.N. (2009). Solvent denaturation of proteins and interpretations of the *M* value. In *Methods in Enzymology*, Vol 466: Biothermodynamics, Pt B, M.L. Johnson, J.M. Holt, and G.K. Ackers, eds. (Elsevier), pp. 549–565.
- Schulman, B.A., Kim, P.S., Dobson, C.M., and Redfield, C. (1997). A residue-specific NMR view of the non-cooperative unfolding of a molten globule. *Nat. Struct. Biol.* **4**, 630–634.
- Schwalbe, M., Ozenne, V., Bibow, S., Jaremko, M., Jaremko, L., Gajda, M., Jensen, M.R., Biernat, J., Becker, S., Mandelkow, E., et al. (2014). Predictive atomic resolution descriptions of intrinsically disordered hTau40 and  $\alpha$ -synuclein in solution from NMR and small angle scattering. *Structure* **22**, 238–249.
- Shen, Y., and Bax, A. (2007). Protein backbone chemical shifts predicted from searching a database for torsion angle and sequence homology. *J. Biomol. NMR* **38**, 289–302.
- Sormanni, P., Piovesan, D., Heller, G., Bonomi, M., Kucic, P., Camilloni, C., Fuxreiter, M., Dosztanyi, Z., Pappu, R., Babu, M.M., et al. (2017). Simultaneous quantification of protein order and disorder. *Nat. Chem. Biol.* **13**, 339–342.
- Soucek, L., Helmer-Citterich, M., Sacco, A., Jucker, R., Cesareni, G., and Nasi, S. (1998). Design and properties of a myc derivative that efficiently homodimerizes. *Oncogene* **17**, 2463–2472.
- van der Lee, R., Buljan, M., Lang, B., Weatheritt, R.J., Daughdrill, G.W., Dunker, A.K., Fuxreiter, M., Gough, J., Gsponer, J., Jones, D.T., et al. (2014). Classification of intrinsically disordered regions and proteins. *Chem. Rev.* **114**, 6589–6631.
- Wiedemann, C., Goradia, N., Häfner, S., Herbst, C., Görlach, M., Ohlenschläger, O., and Ramachandran, R. (2015). HN-NCA heteronuclear TOCSY-NH experiment for (<sup>1</sup>H)(<sup>15</sup>N) and (<sup>15</sup>N) sequential correlations in ((<sup>13</sup>C), (<sup>15</sup>N) labelled intrinsically disordered proteins. *J. Biomol. NMR* **63**, 201–212.
- Wright, P.E., and Dyson, H.J. (2015). Intrinsically disordered proteins in cellular signalling and regulation. *Nat. Rev. Mol. Cell Biol.* **16**, 18–29.
- Yin, X., Giap, C., Lazo, J.S., and Prochownik, E.V. (2003). Low molecular weight inhibitors of Myc-Max interaction and function. *Oncogene* **22**, 6151.
- Zhang, O.W., Kay, L.E., Shortle, D., and Forman-Kay, J.D. (1997). Comprehensive NOE characterization of a partially folded large fragment of staphylococcal nuclease Delta 131 Delta, using NMR methods with improved resolution. *J. Mol. Biol.* **272**, 9–20.

## STAR★METHODS

## KEY RESOURCES TABLE

REAGENT or RESOURCE	SOURCE	IDENTIFIER
<b>Bacterial and Virus Strains</b>		
BL21 (DE3) Gold <i>E. coli</i> .	Agilent technologies	CAT# 230132
<b>Chemicals, Peptides, and Recombinant Proteins</b>		
Human Myc protein (RRID:SCR_008608) C-terminal domain (bHLH-LZ) residues 351-437	In-house	N/A
<sup>13</sup> C glucose	Sigma Aldrich	CAT# 389374
<sup>15</sup> N ammonium chloride	Sigma Aldrich	CAT# 299251
Guanidinium Chloride	Sigma Aldrich	CAT#G4505
TEV protease	In-house	N/A
Talon Co2+ affinity column	Sigma Aldrich	CAT#GE28-9575-02
Complete Protease inhibitors	Roche	CAT# 11697498001
MTSL (1-Oxyl-2,2,5,5-tetramethyl-?3-pyrroline-3-methyl) Methanethiosulfonate	Toronto Research Chemicals	CAT#O875000
<b>Deposited Data</b>		
Backbone 1H, 13C, and 15N Chemical Shift Assignments for the Myc bHLH-LZ domain in presence of 3.2 M GdmCl	This paper	BMRB: 27701
Backbone 1H, 13C, and 15N Chemical Shift Assignments for the Myc bHLH-LZ domain in presence of 2.4 M GdmCl	This paper	BMRB: 27702
Backbone 1H, 13C, and 15N Chemical Shift Assignments for the Myc bHLH-LZ domain in presence of 1.6 M GdmCl.	This paper	BMRB: 27703
Backbone 1H, 13C, and 15N Chemical Shift Assignments for the Myc bHLH-LZ domain	This paper	BMRB: 27704
Crystal structure of Myc-Max recognizing	( <a href="#">Nair and Burley, 2003</a> )	PDB: 1nkp
Structural ensemble of Myc bHLH-LZ domain consistent with NMR data	This paper	DOI: <a href="https://doi.org/10.17632/xhdwd26fdc.1">10.17632/xhdwd26fdc.1</a>
Backbone 1H, 15N Chemical Shift Assignments for the Myc bHLH-LZ domain as a function of GdmCl concentration.	This paper	DOI: <a href="https://doi.org/10.17632/xhdwd26fdc.1">10.17632/xhdwd26fdc.1</a>
Backbone 1H, 15N Chemical Shift Assignments for the Myc bHLH-LZ domain as a function of NaCl concentration.	This paper	DOI: <a href="https://doi.org/10.17632/xhdwd26fdc.1">10.17632/xhdwd26fdc.1</a>
PREs as used in structure model selection	This paper	DOI: <a href="https://doi.org/10.17632/xhdwd26fdc.1">10.17632/xhdwd26fdc.1</a>
Backbone 1H, 13C, 15N Chemical Shift Assignments for the Myc bHLH-LZ domain as used in structure model selection	This paper	DOI: <a href="https://doi.org/10.17632/xhdwd26fdc.1">10.17632/xhdwd26fdc.1</a>
PREs for 3 variants (365-SL, 386-SL and 405-SL) as a function of GdmCl concentration.	This paper	DOI: <a href="https://doi.org/10.17632/xhdwd26fdc.1">10.17632/xhdwd26fdc.1</a>
<b>Recombinant DNA</b>		
6xHis-Tagged-Myc-351-437	This paper	N/A
<b>Software and Algorithms</b>		
Topspin 3.5	Bruker	N/A
CCPN Analysis 2.3	CCPN	N/A
Numeric python routines		N/A
Flexible Meccano	<a href="#">Ozenne et al., 2012</a>	N/A
Asteroids	<a href="#">Salmon et al., 2010</a>	N/A
SPARTA	<a href="#">Shen and Bax, 2007</a>	N/A

## LEAD CONTACT AND MATERIALS AVAILABILITY

Further information and requests for resources and reagents should be directed to and will be fulfilled by the Lead Contact, Jonathan Waltho ([j.waltho@manchester.ac.uk](mailto:j.waltho@manchester.ac.uk)).



## EXPERIMENTAL MODEL AND SUBJECT DETAILS

Experimental model is recombinant, human Myc protein (RRID:SCR\_008608) C-terminal domain (bHLH-LZ) residues 351-437. It was expressed in *E. coli* BL21(DE3) Gold from a pET -derived vector with an N-terminal HisTag, which was removed by proteolysis during purification. Standard conditions were defined as 20 mM phosphate buffer, pH=6.5, T=278 K, with protein concentration 5mg/ml (410  $\mu$ M).

Four single cysteine mutants were prepared for site-specific electron spin-labelling; Q365C, N386, S405C and Q411C.

## METHOD DETAILS

The bHLH-LZ domain of Myc (residues 351-437) and the cysteine point-mutants were expressed from a pET derived vector in *E. Coli* BL21 (DE3) Gold cell lines (Agilent Technologies) at 37°C (310 K) in M9 minimal medium supplemented with 2 g/L of  $^{13}$ C glucose (or 4 g/L of  $^{12}$ C glucose) and 1 g/L  $^{15}$ N ammonium chloride (Sigma-Aldrich) as the only carbon and nitrogen sources. Protein expression was induced by addition of 0.1 mM IPTG to bacterial cultures at OD<sub>600</sub>=0.9, which were harvested 4 h after induction and frozen at -80°C. Cell pellets were resuspended in 20 mM phosphate buffer with 8 M urea and protease inhibitor tablet "Complete" (Roche), sonicated and centrifuged for 30 min at 40000 g. Supernatant was loaded on a Talon Co<sup>2+</sup> affinity column, equilibrated with 3 M GdmCl, 20 mM phosphate, 0.1 M NaCl, pH=7.4, washed by 2.5 mM imidazole and Myc was eluted by addition of 125 mM imidazole. The His-tag was cleaved off by TEV protease and the resulting His-tag peptides were removed by further Co<sup>2+</sup>-affinity chromatography. The purity and identity of the proteins were validated by electrospray ionization mass spectrometry (ESI-MS) and SDS-PAGE.

Paramagnetic labelling of Myc was achieved by incubating Myc cysteine mutants with MTSL (S-(1-oxyl-2,2,5,5-tetramethyl-2,5-dihydro-1H-pyrrol-3-yl)methyl methanesulfonylthioate; Toronto Research Chemicals, Canada) in the presence of 3 M GdmCl and 1 mM DTT at RT in the dark for 8 h. MTSL was present in 5:1 excess over the total thiol concentration. Reaction completeness was confirmed by mass-spectrometry to be more than 95%. Samples were buffer exchanged in 20 mM phosphate, 1 mM EDTA, pH 6.5.

Buffer conditions were screened and optimized to provide best spectral dispersion, highest signal intensity and least visible aggregation for Myc samples. The buffer screen covered pHs from 5 to 7.5 and NaCl concentrations up to 1.2 M, and used either phosphate or Bis-Tris to control pH. The effect of temperature was also studied. Standard conditions were defined as 20 mM phosphate buffer, pH=6.5, T=278 K, with protein concentration 5mg/ml (410  $\mu$ M).

All samples for NMR spectroscopy were prepared in 20 mM phosphate buffer, pH=6.5 and varying concentration of GdmCl with addition of 10% D<sub>2</sub>O and 1 mM TSP (Trimethylsilyl propanoic acid). Except where stated, spectra were recorded at 278 K on a Bruker AVANCE III 800 MHz spectrometer equipped with a TCI cryoprobe ( $^1$ H- $^{13}$ C/ $^{15}$ N with z-gradients) in 3mm tubes. Gradient selective, sensitivity-enhanced HSQC spectra had a spectral width of 20 ppm (1622 Hz) and apparent acquisition time of 60 ms for the indirect dimension. Spectra were processed using Topspin 3.2 software (Bruker Corp).

Protein backbone resonance assignment experiments were recorded for Myc at 3.2 M GdmCl, comprising two-dimensional  $^{15}$ N- $^1$ H HSQC and triple resonance experiments (H)N(CA)NNH, HNCACB, HNCA, HNCO, HN(CO)CA and HN(CO)CACB spectra. All spectra were collected using Echo/Antiecho-TPPI gradient selection, which was efficient at suppressing signals from GdmCl and other buffer components. Non-uniform sampling (NUS) was used to optimize resolution of the indirect dimensions in the available experiment time. NUS acquired data were processed using MDD algorithm within Topspin. Spectra were visualised and analysed using CCPN Analysis 2.3.

Two-dimensional  $^1$ H- $^{15}$ N HSQC spectra were collected at a range of GdmCl concentrations (from 0 to 3.2 M with 0.2 M step). In order to confirm validity of the resonance assignment transfer between denaturant concentrations HNCACB spectra were collected for 2.4, 1.6 and 0 M GdmCl. This led to unambiguous assignment of Myc at native-like conditions even for very low intensity peaks. In addition, a sodium chloride titration of Myc between 0 and 1.2 M (with 0.2 M step) was collected. To characterize the Myc self-association and aggregation, protein concentrations (0, 0.025, 0.05, 0.1, 0.2, 0.4, 0.8 mM) were varied and  $^1$ H- $^{15}$ N HSQC spectra recorded, repeated at 0, 0.6, 1 and 2 M GdmCl.

Paramagnetic relaxation enhancement (PRE) data were collected for diamagnetic and paramagnetic samples at a range of GdmCl concentrations (0 to 3.2 M with 0.3 M step). Diamagnetic sample was obtained by addition of a 5-fold excess of sodium L-ascorbate to the spin-labelled protein sample. Relaxation delays for  $^{15}$ N- $^1$ H HSQC were 2 s, which was sufficient to allow 90% signal recovery between transients.

## QUANTIFICATION AND STATISTICAL ANALYSIS

Data were processed in Topspin 3.2 and quantified in CCPN Analysis 2.3. Data fitting was by Levenberg-Marquadt non-linear least squares optimisation using in-house routines interfacing with Numerical Python.

Chemical shifts were analysed as follows: the total reaction scheme for the interaction between Myc and GdmCl can be described by [Scheme 1](#), as shown in the main text. Because the aggregation process is slow and irreversible, it doesn't contribute to chemical shifts. In addition, the dissociation constant for Gdm<sup>+</sup> binding to the unfolded state is so high (>4M) that the effect can be approximated by a linear function. Thus, the chemical shift data can be analysed according to the following simplified scheme:

$K_{D(Cl)}$  is the binding constant for chloride and  $K_{N/D}$  is equilibrium constant between the denatured and the native disordered states. Proton chemical shift perturbation dependence by GdmCl was fitted to equation:



$$\delta H_i = \delta H_0 + \frac{\frac{[GdmCl]}{K_D} * (\Delta\delta H_{Cl} + (\Delta\delta H_{Gdm} + slope_H * [GdmCl]) * K)}{1 + \frac{[GdmCl]}{K_D} * (1 + K)} \quad \text{with } K = K_0 * e^{-m \cdot [GdmCl]} \quad (\text{Equation 1})$$

$\delta H_0$  is the initial value of the proton chemical shift difference for residues,  $\Delta\delta H_{Cl}$  is the maximum chemical shift perturbation of the proton chemical shift by chloride and  $\Delta\delta H_{Gdm}$  is the maximum effect of Gdm.  $K_0$  is the value of  $K$  at 0 M GdmCl,  $m$  is the denaturant concentration dependence of the free energies.  $^{15}\text{N}$  chemical shifts were fitted to the same equation. Initial fitting was to a subset of residues with clearly defined behaviour, fitting a  $K_D$ ,  $K_0$  and  $m$  as global parameters, and chemical shifts on a per residue basis. Subsequently, the values of  $K_D$ ,  $K_0$  and  $m$  were fixed in fits of all residues. No significant difference between the fit-lines and the data points resulted. The efficacy of using the global parameters to allow extrapolation to zero denaturant for residues with significant signal attenuation under such conditions was tested by omitting data points below 0.6 M GdmCl for complete data sets and repeating the fitting procedure. The RMS deviation between the fitted values and the recorded chemical shifts was 0.03 ppm for  $\delta H$  and 0.3 ppm for  $\delta N$ . These uncertainties were propagated into the estimates of  $^{13}\text{C}$  chemical shifts.

$^{13}\text{C}_\alpha$  and  $^{15}\text{N}_H$  chemical shifts changes for each residue were found to correlate, and so the maximum  $^{15}\text{N}$  shift defined by data fitting was used to calculate the  $^{13}\text{C}_\alpha$  shifts at 0 M GdmCl used for SSP. For residues with complete datasets, omitting the 0 M GdmCl point and repeating the process gives a RMS difference from the recorded value of 0.37 ppm for  $C_\alpha$  (0.23 after excluding outliers H359 and F375) and similarly 0.75 ppm for  $C_\beta$  (0.23 after excluding the same outliers). Neither of these outlier residues are in regions with strong secondary structure propensity.

PRE effects were calculated from the intensity ratio of HSQC peaks between paramagnetic and diamagnetic samples for each residue, and fitted to the following equation (Cliff et al., 2009).

$$\frac{I_{ox}}{I_{red}} = \frac{R'_2}{R'_2 + R'_p} e^{-(R'_p \cdot t)} \quad \text{where } R'_x = \frac{R_x^D + R_x^N * K}{(1 + K)} \quad \text{with } K = K_0 * e^{-m \cdot [GdmCl]} \quad (\text{Equation 2})$$

The exchange between conformers is fast relative to the chemical shift timescale, and therefore assumed to be fast on the  $^1\text{H}$ -e relaxation timescale, and therefore the apparent transverse relaxation rate in diamagnetic samples ( $R_2^D$ ) and the additional paramagnetic relaxation rate ( $R_p^N$ ) are population weighted averages between the rates in the native, denatured state (N) populated at 0 M GdmCl, and the denatured state (D) populated at high GdmCl concentrations. The time  $t$  is the amount of time protons are transverse in the HSQC pulse sequence, amounting to 10.6 ms.  $R_2^D$  was fixed at 7 Hz ( $\times 2\pi$ ) and residue specific  $R_2^N$  values were estimated from the guanidinium dependence of the intensities in the diamagnetic sample. These needed correcting for the change in sensitivity of the probe with  $\text{Cl}^-$  concentration, which is proportional to the change in proton pulse-length ( $\rho_D/\rho_{0M}$ ).

$$I_{red,D} = I_{red,0M} \times \frac{\rho_D}{\rho_{0M}} \times \frac{R'_2 e^{-(R'_2 - R_2^D) \cdot t}}{R_2^D} \quad (\text{Equation 3})$$

with  $R'_2$  calculated as in Equation 2.

### Ensemble Calculation

An original ensemble created by *flexible meccano* (Ozenne et al., 2012; Salmon et al., 2010) comprised 10,000 structures with the phi/psi angles corresponding to random coils. 50 random ensembles with 200 structures each were created and  $\chi^2$  values were calculated for each ensemble. Then using ASTEROIDS (Salmon et al., 2010) genetic algorithm 5 ensembles with 200 structures each were selected on the basis of the best fit to the experimental chemical shift data. SPARTA (Shen and Bax, 2007) was used for prediction of chemical shifts. From these structures, 1000 phi/psi angles were extracted for each residue, which were used as a library to build 8500 structures for the next iteration. Next iteration started with 8500 structures from the previous calculation and 1500 structures created from the random coil library. This process was repeated 5 times to avoid being trapped in local minima.

These final 10000 structures were used as a starting pool to fit the PRE and chemical shift data simultaneously. ASTEROIDS was used to produce equivalent ensembles containing 100 structures (5000 evolution steps were used in the genetic algorithm). PREs were calculated from  $^1\text{H}$   $R_2$  values estimated from the  $^1\text{H}$ -e distance in each conformation, the INEPT delay, the conformational sampling of the spin label relative to the backbone and the estimated correlation time of the dipole interaction (5ns), as described elsewhere (Salmon et al., 2010).

Long-range order was assessed in the final ensembles by calculating distance values normalized against the average distance values calculated for the chemical shift (CS) based ensemble:

$$\Delta_{ij} = \log \left( \frac{d_{ij}}{d_{ij}^0} \right)$$

where  $d_{ij}$  is the distance between residues  $i$  and  $j$  in the final (CS-PRE) calculated ensemble and  $d_{ij}^0$  is distance between residues  $i$  and  $j$  for the CS calculated ensemble. These values were used to plot contact map.

#### **DATA AND CODE AVAILABILITY**

NMR chemical shifts have been deposited with the BioMagResBank with accession codes 27701, 27702, 27703 and 27704.

**Structure, Volume 27**

**Supplemental Information**

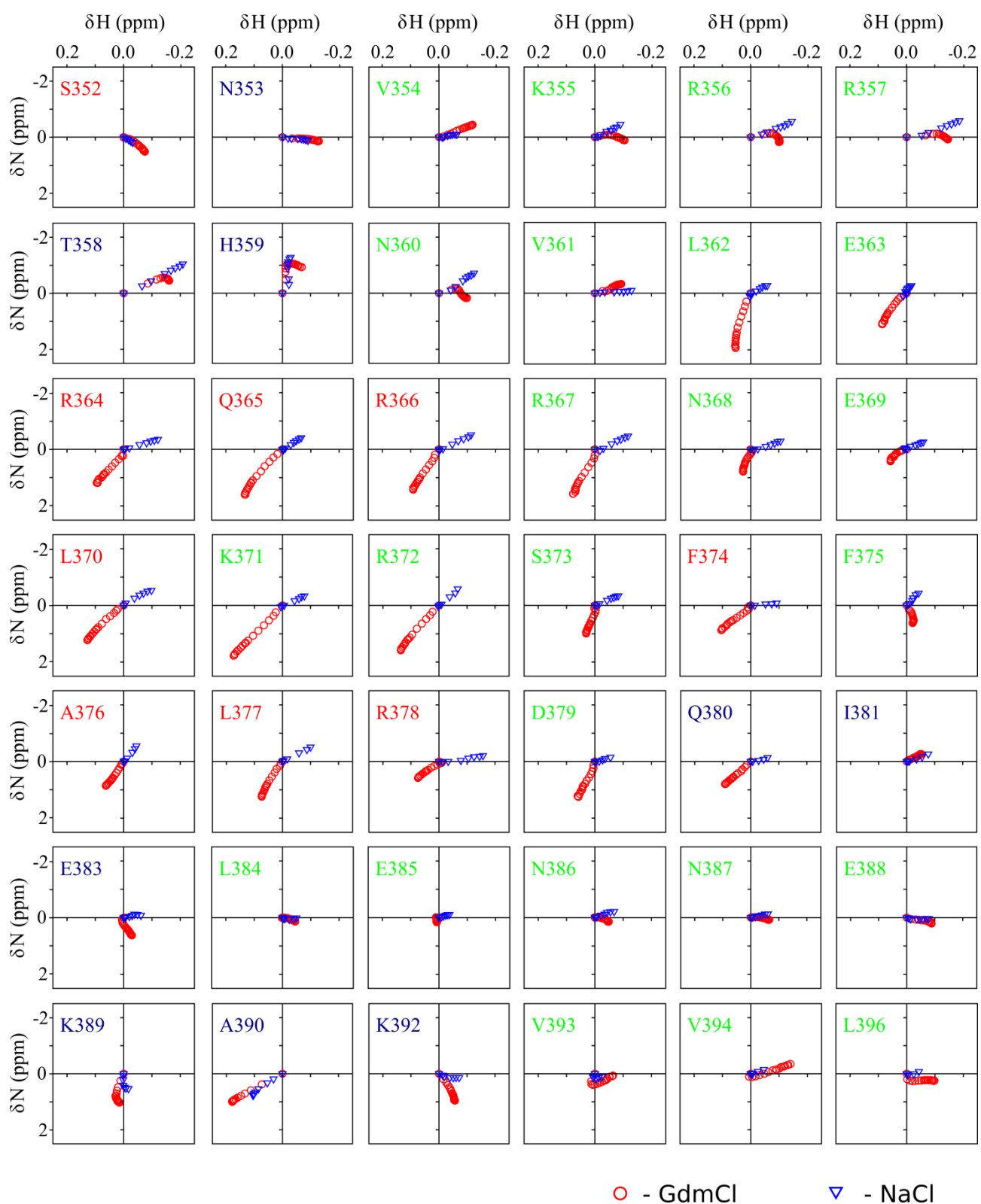
**Mapping Hidden Residual Structure**

**within the Myc bHLH-LZ Domain**

**Using Chemical Denaturant Titration**

**Stanislava Panova, Matthew J. Cliff, Pavel Macek, Martin Blackledge, Malene Ringkjøbing Jensen, J. Willem M. Nissink, Kevin J. Embrey, Rick Davies, and Jonathan P. Waltho**

## Supplemental Data



○ - GdmCl      ▽ - NaCl

**Figure S1:** (relates to **Fig. 2**) The behaviour of observable  $^1\text{H}$ ,  $^{15}\text{N}$  correlation peaks in HSQC spectra of Myc over a GdmCl titration and a NaCl titration. GdmCl concentration range (red circles): 0.0 to 3.2 M, with 0.2 M steps. NaCl concentration range (blue triangles): 0.0 to 1.2 M, with 0.2 M steps. Residue names are coloured as in Fig. 1.



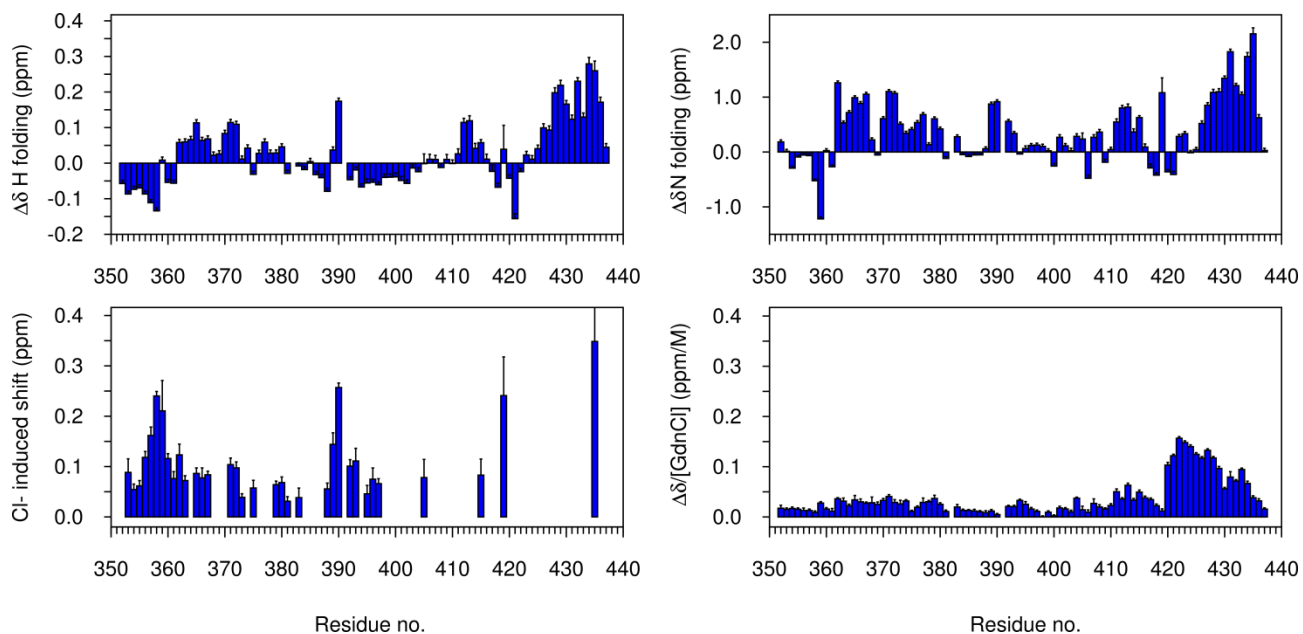


**Figure S2** Relates to **Fig 2**. Values of best fit residue-specific parameters for proton (top-left) and nitrogen (top-right) chemical shift for the sigmoidal transition ( $\Delta\delta H_{\text{folding}}$  and  $\Delta\delta N_{\text{folding}}$ ), the Cl<sup>-</sup> induced hyperbolic transition (expressed as  $((\Delta\delta H_{\text{Cl}})^2 + (\Delta\delta N_{\text{Cl}}/6)^2)^{0.5}$ , bottom-left) and the slope of final shallow transition (bottom-right).

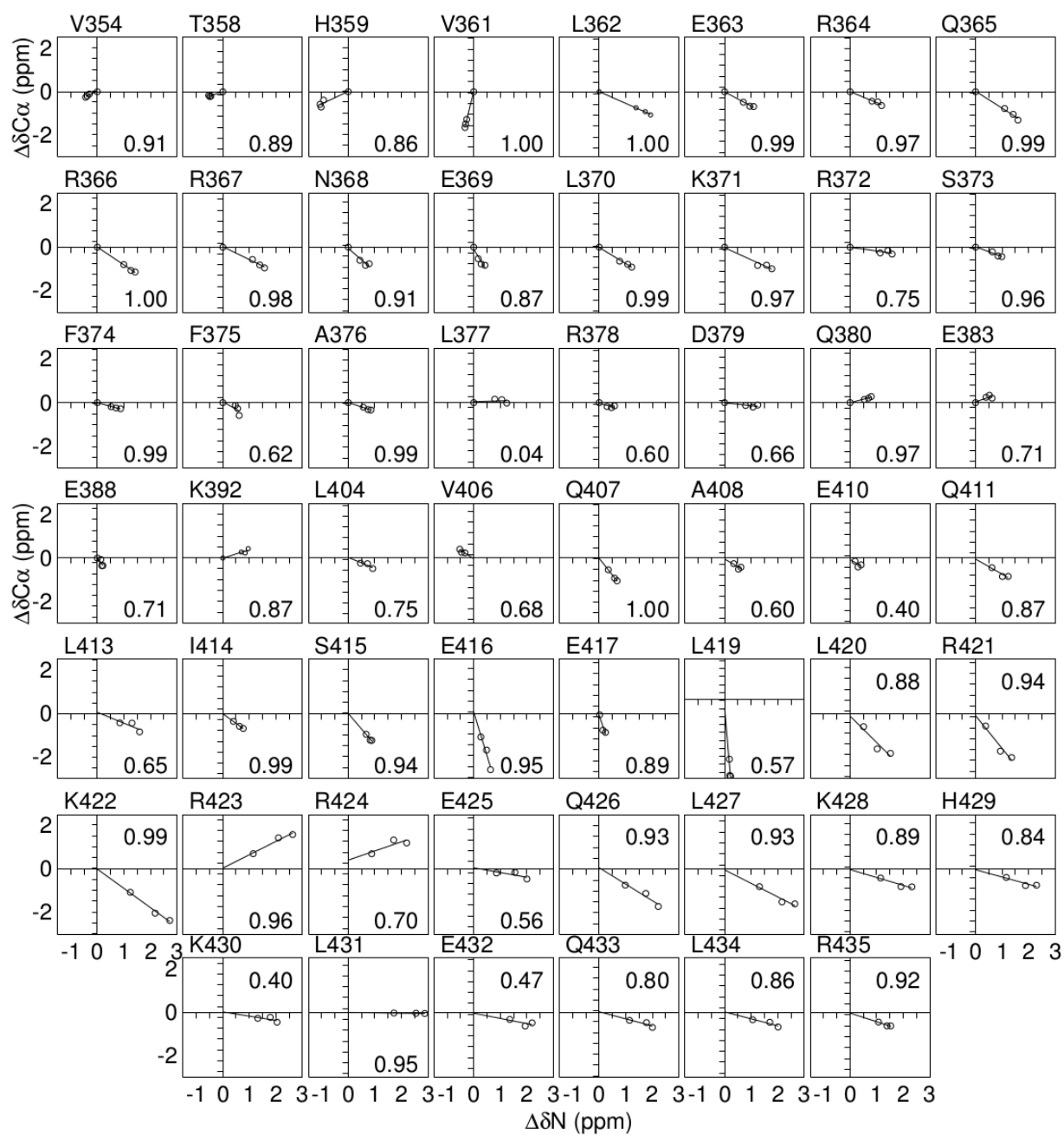


**Figure S3:** relates to **Fig. 3**,  $\bar{\delta}C_{\alpha}$  plotted against  $\Delta\bar{\delta}N$  for representative residues. Correlation coefficients are shown inset for each residue.

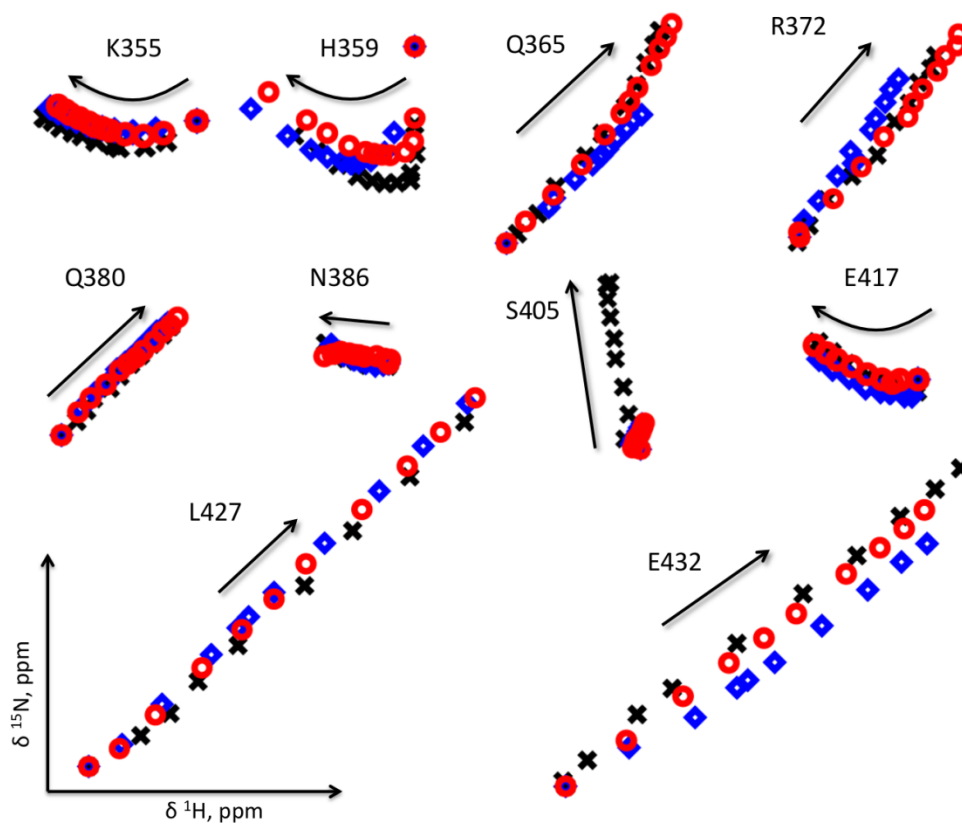


**Figure S4:** relates to **Fig. 4**. Denaturation profiles mapped as cross-peaks from  $^1\text{H}$ - $^{15}\text{N}$  HSQC spectra for the different Myc cysteine mutants: Q365C (blue diamonds), N386 (red circles), S405 (black crosses). The radii of the circles (dimensions of crosses and squares) correspond to 0.015 ppm in the  $^1\text{H}$  dimension HSQC spectra. Arrows point in the direction of the cross-peak motion upon increasing GdmCl concentration.

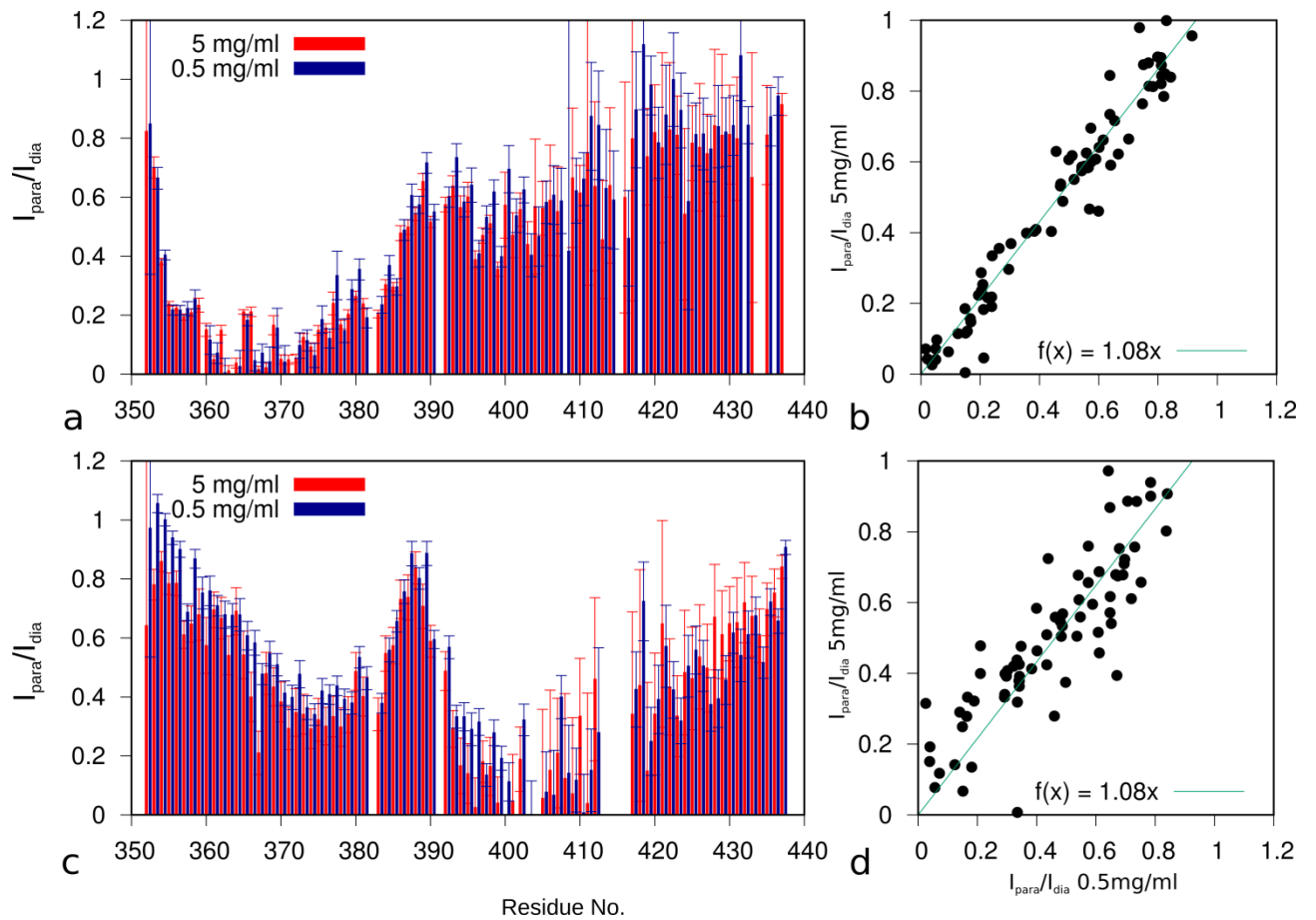


**Figure S5:** relates to **Fig 5**. Sequence distribution of PREs ( $I_{para}/I_{dia}$ ) at 0.5 (blue) and 5 (red) mg/ml at 0.6 M GdmCl, for Q365C (A) and S405C (C) spin-labelled variants. PRE ratios of 0.5 mg/ml vs 5 mg/ml were plotted to illustrate correlation between them (B and D) and regression coefficient (slope value).

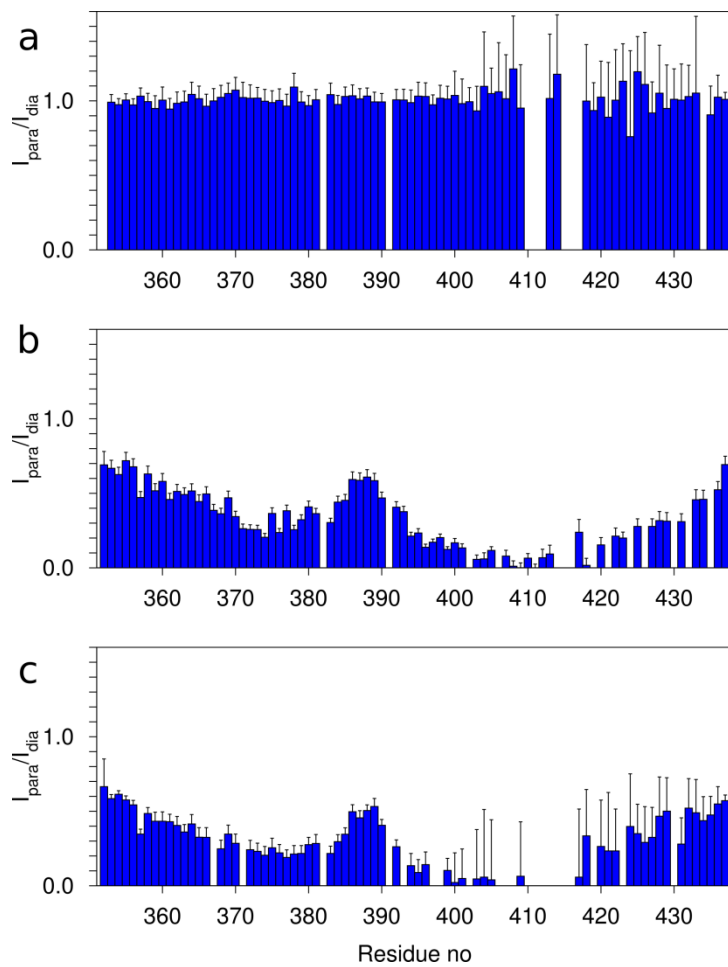


**Figure S6:** Relates to **Fig. 5**. Intensity ratios of samples with paramagnetic MTSL to diamagnetic MTSL when **a)**  $^{14}\text{N}$ -Myc Q411-MTSL is in 1:1 mix with underivatized  $^{15}\text{N}$  Myc Q411 at 4 mg/ml **b)**  $^{15}\text{N}$ -Myc Q411-MTSL at the same concentration. **c)**  $^{15}\text{N}$ -Myc S405-MTSL at the same concentration



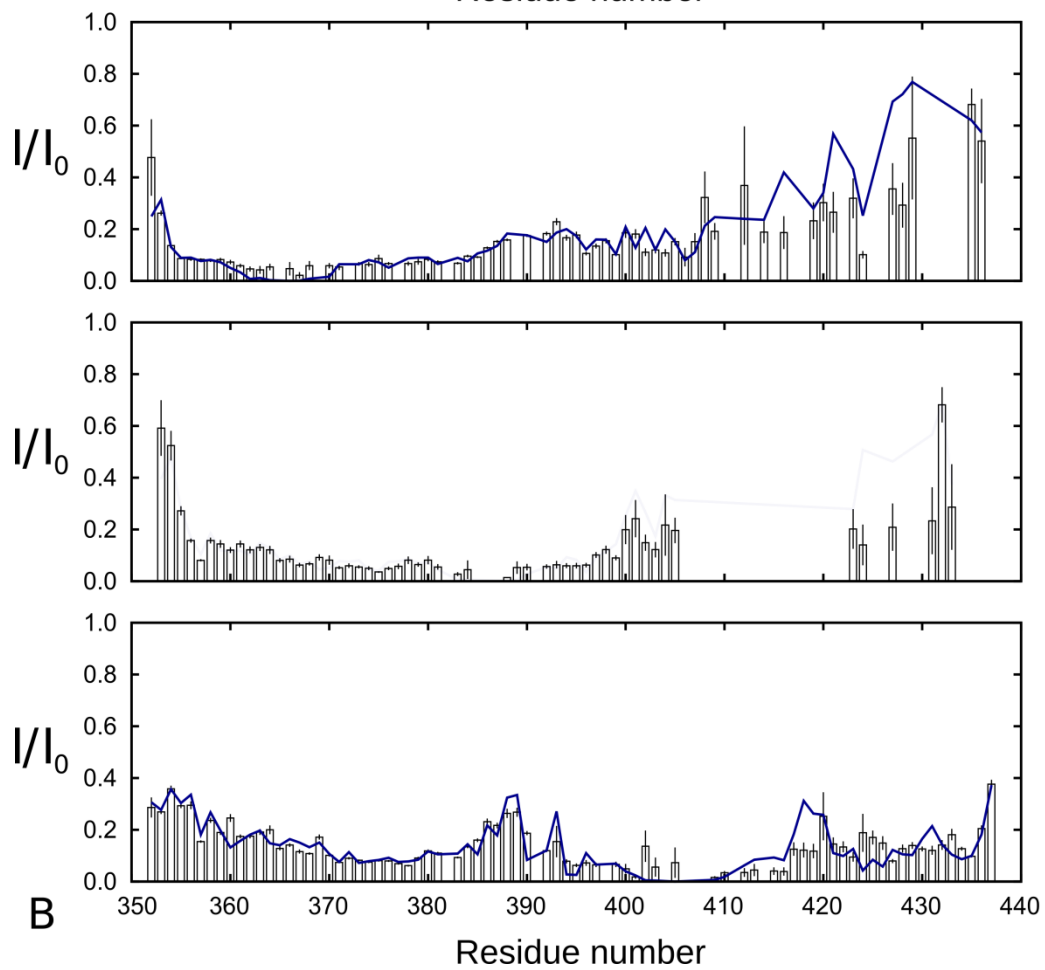
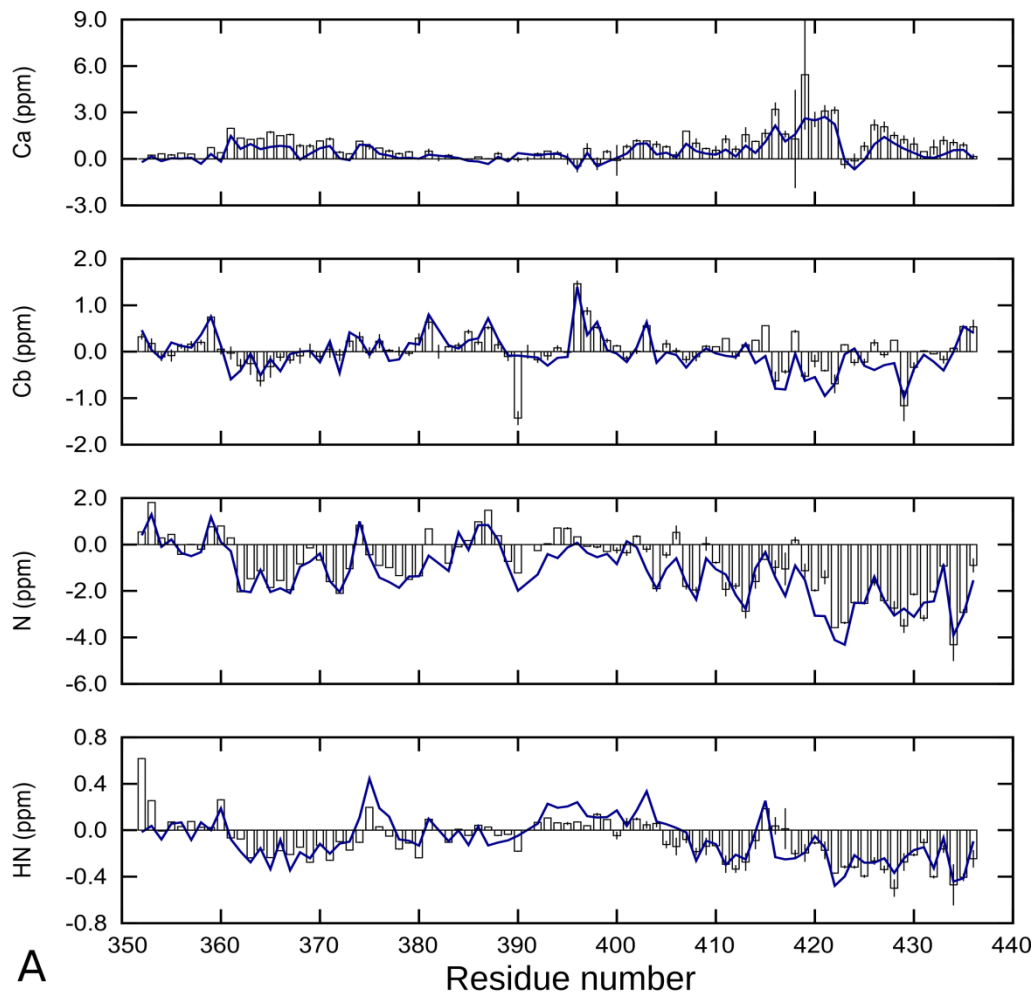


**Figure S7:** Relates to **Fig. 6 & 7**. Comparison of the experimental (empty bars) and ensemble averaged data (blue line) for Myc at 0 M GdmCl. (A) Chemical shift deviation from random coil values back-calculated by SPARTA; (B) Intensity ratios between paramagnetic and diamagnetic samples on a per residue level.